Accepted Manuscript

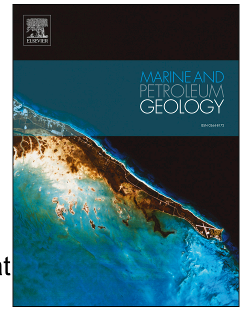

Deep-seated faults and hydrocarbon leakage in the Snøhvit Gas Field, Hammerfest Basin, Southwestern Barents Sea

S.M. Mohammedyasin, S.J. Lippard, K.O. Omosanya, S.E. Johansen, D. Harishidayat

PII: S0264-8172(16)30194-5

DOI: 10.1016/j.marpetgeo.2016.06.011

Reference: JMPG 2592

To appear in: *Marine and Petroleum Geology*

Received Date: 5 August 2015

Revised Date: 7 June 2016

Accepted Date: 13 June 2016

Please cite this article as: Mohammedyasin, S.M., Lippard, S.J., Omosanya, K.O., Johansen, S.E., Harishidayat, D., Deep-seated faults and hydrocarbon leakage in the Snøhvit Gas Field, Hammerfest Basin, Southwestern Barents Sea, *Marine and Petroleum Geology* (2016), doi: 10.1016/j.marpetgeo.2016.06.011.

Deep-seated faults and hydrocarbon leakage in the Snøhvit Gas Field, Hammerfest Basin, Southwestern Barents Sea

Mohammedyasin S.M[1], Lippard, S.J[1], Omosanya, K.O[2], Johansen, S.E[2], Harishidayat, D[2]

[1]Department of Geology and Mineral Resources Engineering,

[2]Department of Petroleum Engineering and Applied Geophysics

Norwegian University of Science and Technology, Trondheim

Corresponding author: kamaldeen.o.omosanya@ntnu.no

Abstract

High-quality 3D seismic data are used to analyze the history of fault growth and hydrocarbon leakage in the Snøhvit Field, Southwestern Barents Sea. The aim of this work is to evaluate tectonic fracturing as a mechanism driving hydrocarbon leakage in the study area. An integrated approach was used which include seismic interpretation, fault modeling, displacement analysis and multiple seismic attribute analysis.

The six major faults in the study area are dip-slip normal faults which are characterized by complex lateral and vertical segmentation. These faults are affected by three main episodes of fault reactivation in the Late Jurassic, Early Cretaceous and Paleocene. Fault reactivation in the study area was mainly through dip-linkage. The throw-distance plots of these representative faults also revealed along-strike linkage and multi-skewed C-type profiles. The faults evolved through polycyclic activity involving both blind propagation and syn-sedimentary activity with their maximum displacements recorded at the reservoir zone. The expansion and growth indices provided evidence for the interaction of the faults with sedimentation throughout their growth history.

Soft reflections or hydrocarbon-related high-amplitude anomalies in the study area have negative amplitude, reverse polarity and are generally unconformable with structural reflectors. The interpreted fluid accumulations are spatially located at the upper tips of the major faults and gas chimneys. Four episodes of fluid migration are inferred and are linked to the three phases of fault reactivation and Neogene glaciations. Hydrocarbon leakage in the Snøhvit Gas Field is driven by tectonic fracturing, uplift, and erosion. The interpreted deep-seated faults are the main conduits for shallow hydrocarbon accumulations observed on seismic profiles.

Keywords: Faults, Hydrocarbon, Migration, Leakage, Snøhvit.

1.0 Introduction

Fluid-flow or migration is associated with excess pore-fluid pressure which can be attributed to varying processes such as rapid sediment loading, uplift and erosion, dissociation of gas hydrate, polygonal faulting, and leakage from source and reservoir rocks (Doré and Jensen, 1996; Gay et al., 2011; Heggland, 1998; Hovland and Judd, 1988; Mienert et al., 2005). Fluid-flow processes are revealed on seismic reflection profiles as seabed pockmarks, mud volcanoes, and methane derived carbonate mounds, and in the subsurface as seismic blow-out pipes, gas chimneys, paleo-pockmarks and amplitude anomalies (Vadakkepuliyambatta et al., 2013). In the Barents Sea, glacial lineations and iceberg plough marks are also related with the presence of gaseous hydrocarbons (Andreassen et al., 2008; Chand et al., 2008).

The flow mechanism can be triggered by the presence of stratigraphic boundaries, leaking faults and an increase in seafloor temperature during fast deposition of glacio-marine sediments (Chand et al., 2012). Out of all these trigger mechanisms, the role of tectonism or faulting in hydrocarbon migration/leakage on continental margins is still poorly understood. In the special case of the Snøhvit Field, uplift and erosion was proposed as the major factor for fluid leakage at the detriment of tectonics and other mechanisms (Cavanagh et al., 2006; Chand et al., 2008). Cavanagh et al. (2006) and Rodrigues Duran et al. (2013) proposed multiphase erosion including glacial erosion, loading/unloading, and Cenozoic exhumation as the main cause of hydrocarbon migration in the Hammerfest Basin. Arvo, 2014 and Ostanin et al., 2013 sparingly discussed the role of fault reactivation and polygonal faulting as mechanisms driving fluid leakage in the area. Hence, there is a pressing need to understand and further investigate the influence of deep-seated faulting as a mechanism for fluid migration in the Hammerfest Basin.

This work is therefore done to elucidate the growth history and displacement character of faults in the Snøhvit field, their mode of reactivation and relationship with fluid migration or leakage. The study area is located in the Hammerfest Basin between the Loppa High to the north and the Finnmark Platform to the south. It is separated from the Loppa High by the Asterias Fault Complex, from the Tromsø Basin to the west by the southern segment of the Ringvassøy-Loppa Fault Complex, and from the Finnmark Platform by the Troms-Finnmark Fault Complex (Fig 1a). In this work, the history of fault growth was investigated using traditional fault displacement plots and the effect of faulting in fluid-leakage is discussed entirely by analyzing several high-amplitude anomalies identified from the seismic cube.

2.0 Geological setting

The tectonic history of the western Barents Sea can be traced back to the Caledonian Orogeny that strikes through northernmost Norway and northeastwards into the Barents Shelf (Barrère et al., 2009; Gernigon et al., 2014; Gudlaugsson et al., 1998; Ritzmann and Faleide, 2007).

The Caledonian fabric is obscured in most parts of the Barents Sea, except on Svalbard, by Late Paleozoic and Mesozoic sedimentary basins (Breivik et al., 2002; Gee et al., 2008). Extensional tectonics during the Late Paleozoic in the western Barents Sea segmented the basins into a fan-shaped array of block-faulted basins separated by highs (Faleide et al., 1984; Gudlaugsson et al., 1998). The Upper Carboniferous to Lower Permian shallow marine carbonate with evaporite deposits are overlain by Upper Permian clastic deposits which formed in response to the Uralian Orogeny (Johansen et al., 1992).

The Triassic crustal extension in the North Atlantic and locally important differential compaction over the Late Paleozoic grabens has played an important role in accommodation space development (Glørstad-Clark et al., 2010). Intense rifting in the Mid Jurassic to Early Cretaceous occurred in the Southwestern Barents Sea (Faleide et al.,1993; 2008). The westward shift in extensional rifting increased the thicknesses of megasequences with time towards the present day continental-ocean boundary in the Southwestern Barents Sea (Klitzke et al., 2014). In the Late Cretaceous to Paleocene, the breakup between Norway and Greenland was taken up by strike-slip movements along the De Geer Zone. The Southwestern Barents Sea margin developed during the Eocene opening of the Norwegian-Greenland Sea (Faleide et al., 2008). The passive margin evolved in response to subsidence and sediment loading during the widening and deepening of the Norwegian-Greenland Sea. Uplift and glacial erosion during the Pliocene to Pleistocene caused deposition of deep marine fans in the adjacent oceanic domains along the northern and western passive margins (Doré and Jensen, 1996; Henriksen et al., 2011).

The Hammerfest Basin was probably initiated by extensional tectonics in the Carboniferous (Berglund et al., 1986). This caused tilting of the Loppa High and Hammerfest Basin in the Late Carboniferous to Early Permian with reactivation of the underlying basement fault trends. Differential basin subsidence with depocenters in the northeastern and southwestern part of the Hammerfest Basin during the Permian coincided with the reactivation of the Troms-Finnmark Fault Complex and showed that the Asterias Fault Complex was not active during this period. This provides evidence that the Hammerfest Basin was structurally continuous with the Loppa High at this time (Berglund et al., 1986).

Early Triassic sediments onlap onto north to south oriented structural highs and indicate tectonic reactivation during this period. The Late Triassic was a period of quiescence and deposition. Evolution of the margin in the Late Triassic to Mid Jurassic was largely controlled by the interplay of tectonic subsidence, eustatic sea level changes and sediment input. The sea level rise during the Mid Jurassic led to the deposition of the Stø Formation (Berglund et al., 1986). This formation is the main reservoir in the Snøhvit field, and represents a tectonically controlled transgressive wave-dominated estuary (Ottesen et al., 2005). Subsequent erosion of structural highs and deposition was restricted to both shallow and deep marine deltas along the northern and southern margins of the basin (Ottesen et al., 2005). However, the initial sediment distribution was controlled by doming accompanied by E-W trending normal faulting (Faleide et al., 1984) and with the formation of horst and graben structures. During the Late Jurassic, the syn-rift Hekkingen Formation was deposited in a deep marine environment and is the main source rock in the entire Barents Sea (Berglund et al., 1986). Marine sedimentation started as a result of transgression of the central part of the Hammerfest Basin during the Mid Paleocene. A SSW progradation of sediment from the platform areas to

NNE of the basin occurred during the Late Paleocene. Subsidence and continued erosion was dominant during the Oligocene and Miocene (Knutsen and Vorren, 1991).

3.0 Data and Methods

This study uses pre-stack time-migrated (PSTM) 3D seismic data covering an area of approximately 486 km^2 in water depths of 250 to 360 m in the Snøhvit Gas Field. The seismic data consists of 825 inlines and 3775 crosslines, each measuring approximately 47 km and 10 km in length respectively. The inlines are oriented in a NNE-SSW direction perpendicular to fault strike, while the crosslines are oriented parallel to fault strike. During data acquisition, a dual airgun was used working at a sampling rate of 4 ms (Nyquist Frequency of 250 Hz). The interpreted seismic volume has bin spacing of 12.5 x 12.5 m. Vertical resolutions (i.e., $\lambda/4$) of the seismic volume are approximately 10 m for shallow horizons and 15 m for deeper stratigraphic units. The lateral resolution is equal to the bin spacing, which is 12.5 m.

The main methods used in this work include: (1) mapping of the horizons, faults, and high-amplitude anomalies (2) fault and horizon modelling (3) fault displacement analysis and (4) multiple seismic attribute analysis using root mean square (RMS) amplitude, variance and chaos and geobody extraction. The first task in mapping the horizons is well-to-seismic tie in which formation tops from the boreholes were linked to their time-equivalent reflectors on the seismic data. The horizons in this work were interpreted using the 2D and 3D auto-tracking tool in Petrel®2015 across individual seismic profiles. Subsequently, the interpretation was extended into the seed grid at inlines and crossline spacing of 10 (equivalent to 125 m). The complete grids were later converted into surfaces in order to generate thickness maps.

Faults were manually interpreted across seismic profiles perpendicular to fault strikes at intervals of 62.5 m (5 inlines or crosslines). Fault displacement data such as the plot of displacement- distance (t-x), throw-depth (t-z), expansion and growth indices, were used to interpret the history of fault growth, linkage and reactivation. The vertical (throw) dip separations were measured at fault cut-off points on the hanging-wall and footwall sections. In order to make throw-depth (t-z) plots, the throw was determined across the faulted horizons and then plotted against depth to the midpoints between the respective hanging-wall and footwall cut-offs (Hongxing and Anderson, 2007; Reeve et al., 2015). These plots provide insights into potential reactivation of faults by dip-linkage (Mansfield and Cartwright, 1996; Tvedt et al., 2013), and also for distinguishing faults that developed through syn-sedimentary activity from those that grow through blind or radial propagation of their tips (Omosanya and Alves, 2014).

Furthermore, the expansion index (EI) and growth index (GI) were used to define the periods of most significant fault growth for normal faults (Thorsen, 1963). EI is the ratio of footwall to hanging-wall strata thickness, while GI is the ratio of the difference in thicknesses between the hanging-wall and the footwall strata divided by the thickness of hanging-wall strata. GI is a measure of relative throw rate to the sedimentation rate in the footwall (Pochat et al., 2009). Fault framework modeling of all the mapped faults was done in the time domain and an average interval velocity of 2 km/s was used to calculate the dip and dip direction of the faults. Graphical analysis of the faults includes the use of rose diagrams and equal area plots to identify the orientation of the faults.

High-amplitude anomalies with opposite or reversed polarity to the seabed reflector are characterized as "soft reflections" i.e., fluid leakages or accumulations in the subsurface (Alves et al., 2015). Once the high-amplitude anomalies were identified, seismic attributes were extracted from the seismic volume to further analyze the high-amplitude anomalies and assess their relationship with stratigraphy or geomorphic features. The seismic attributes used include RMS amplitude, chaos, and the geobody extraction. Root Mean Square (RMS) amplitude was computed between the horizons and used to detect the occurrence of high-amplitude anomalies (HAA). RMS amplitude is calculated as the square root of the sum of the squared amplitudes divided by the number of samples (Brown, 2004). The RMS amplitudes combined the effect of positive and negative amplitude that is possibly due to the presence of hydrocarbons or other fluids. Hence, RMS amplitude seismic attributes are sensitive to sandstone-bearing depositional systems or fluids in a siliciclastic environment (Brown, 2004). Chaos attribute maps the chaotic signal pattern contained within a unit of seismic data and it is a measure of the "lack of organization" in the dip and azimuth estimation method. Chaos in the signal can be affected by gas migration paths, salt body intrusions, and for seismic classification of chaotic texture. The combined attributes were used to show the fluid migration pathways, delineate gas chimneys and static fluid accumulations.

Results

4.1 Seismic stratigraphy of the study area

Eleven interpreted horizons were used to divide the stratigraphy of the study area into ten units (Figs. 2 and 3). These units reflect the influence of faulting and presence of soft reflections. Thickness variation across the faulted sequence is displayed using Two Way Travel Time (TWTT) thickness maps (Fig. 4). The lowermost Unit 1 is Carboniferous in age

(Gabrielsen et al., 1990). Unit 1 is composed of both siliciclastic deposits and carbonates (Ohm et al., 2008). Units 2 and 3 consist of Permian rocks, while Unit 4 includes the Triassic Fruholmen, Snadd, and Kobbe Formations (Ohm et al., 2008). The reservoir zone is Unit 5a, which consists of Tubåen, Nordmela and Stø Formations from bottom to top (Fig. 2). The thickness of the reservoir zone varies from 150 to 400 m (Fig. 4d). Unit 5b comprises the Middle Jurassic to Lower Cretaceous Fuglen, Hekkingen and Knurr Formations. Units 6 to 8 comprise the Kolje, Kolmule and Kviting Formations (Fig. 2). Unit 9 represents the Torsk Formation (Figs. 2 and 3). The horizon (Ha) at the top of the unit marks the upper tips of the major faults, gas chimneys and the shallowest soft reflections. The topmost unit in the study area is Unit 10. The base of Unit 10 corresponds to the Upper Regional Unconformity (URU), which marks the commencement of Pliocene-Pleistocene glaciations in the entire Barents Sea.

4.2 Interpreted faults

Based on their depth of occurrence, the interpreted faults are: (1) Type A or major faults, which are faults offsetting the reservoir zone and extending down to the Triassic, Permian and Carboniferous formations. They are the deep-seated faults numbered F1 to F6 in Figs. 3, 4 and 5a; (2) Type B or intermediate faults, which are common within the Paleocene to Pliocene Formations (Fig. 5b), and (3) Type C or minor faults interpreted within the Late Cretaceous and Eocene intervals (Fig. 5c). The major faults are extensive laterally (i.e. > 10 km in length) and are vertically continuous down to depths of 3000 m and more (Fig. 3 and 6). The intermediate and minor faults are found at shallow depths (Figs. 3, 5b and 5c).

Furthermore, Type A faults strikes mainly in E-W, NE-SW and ENE-WSW directions, with dips to the SE and NW (Fig. 5a). The E-W faults are bounding the Snøhvit field to the north and south. On the other hand, the NE-SW striking faults tip out upward to shallower depths

(600 ms TWTT) and downward to the Carboniferous formations. Prominent fault drag was observed along some of the major faults within Units U6 and U5. This includes both normal and reverse drags occurring along horizons H4, H5 and H6 (Fig. 6).

4.3 Displacement analysis for the major faults

Throw versus depth (t-z) profile

F1 has a gentle negative t-z gradient (-3.4) and decreases in throw with depth from its basal tip to horizon H8 (Fig. 7a). F1 has its maximum throw of ~140 m on horizon H5 and up from H3 the gradient is steep and the throw decreases up to minimum of ~10 m and zero at the upper tips (Fig. 7a). The lower parts of F2 and F1 have similar t-z profiles. F2 has a negative t-z gradient (~5.5) and decreases in throw as depth increases, although with an increase in throw from its base to H4. Maximum throw of ~130 m was estimated for F2 at H5 (Fig. 7b).

F3 has a very gentle t-z gradient at its lower part and decreases in throw upward. Below H4, the gradient becomes steep, negative (~2.8), and later increases further to H5. The maximum throw of ~65 m was measured at H5 (Fig. 7c). Fault 4 (F4) has a steep gradient on its lower part with a maximum throw of ~70 m on H5. The throw decreases from H6 upward and becomes zero at H7 (Fig. 7d). Similarly, F5 has a steep negative gradient at its lower part and the throw increases towards H4 with maximum of ~110 m between H4 and H5 (Fig. 7e). The throw decreases from H5 to its upper part with a positive t-z gradient. F6 and F4 have positive t-z gradients throughout their profiles and with gentle gradients in the lower parts, which decrease toward the middle part of the profiles (Fig. 7d and 7f).

The t-z profiles show complex vertical segmentation of the faults. The profiles include skewed C-type (F1, F2 and F5), C-type (F4) and M-type (F3 and F6) profiles (Fig. 7). Displacement minima indicative of dip-linkage are seen on three faults (F1, F4, and F6). In addition, all the faults show little or no variation in the location of their point of maximum displacement (d_{max}). The point of d_{max} for all the faults is at H5 except for fault F6 that has it d_{max} at H3 (Fig. 7).

Displacement versus distance (t-x)

The displacement-distance (t-x) plots for the major faults show multiple segments along strike on horizons H4, H5 and H6 (Fig. 8). The t-x profiles include multi-skewed C-type profiles and with variable maximum displacement (d_{max}) on each of the horizons (Fig. 8). F1 has maximum displacement on horizon H5, with the d_{max} at the center, which becomes zero towards the tips. Displacement for F2 is frequently changing along H4 (Fig. 8a). The t-x plot for F2 along H5 increases from its origin and reaches up to 370 m maximum displacement (Fig. 8a). The t-x plots for F2 are similar to F1 on horizons H5 and H6. However, an increase in gradient is noted towards H6 (Fig. 8a).

F3 has t-x plots that generally increase with the distance from the origin (Fig. 8a). These plots have distinctive segments. Maximum displacement of up to 700 m was estimated for F3 on H5 (Fig. 8a). In contrast to F3, the t-x plots for F4 and F5 show decreasing displacement from the origin (Fig. 8b). Maximum displacements of about 550 m and 100 m are estimated along H5 for F4 and F5, respectively. However, both faults exhibit multiple segments at different stratigraphic levels (Fig. 8b). F6 has the simplest t-x profile with maximum displacement also noted on H5. Generally, the t-x plot includes the C-type (F1, F2), skewed C-type (F3, F4 and F5) and M-type (F6) profiles of Muraoka and Kamata (1983).

Expansion and growth indices

F1 has expansion indices greater than 1 for U5, U6 and U8 which implies thickening of sediments in the hanging-wall section of the fault (Fig. 9). No change in EI was observed for units U4 and U7 while strata thinning at U9 is signified by EI < 1 (Fig. 9). The maximum expansion index of F1 occurs on U5b. The maximum growth index was recorded on U8 (GI = 0.018; Fig. 10). The expansion indices along F2 show thickening of hanging-wall strata on Unit 5 and no change in thickness from U6 to U9 (Fig. 9). In contrast, the growth index of U5 is negative and > 0 from U7 to U9. For F3, the expansion indices are almost 1 on all of the units except U5. The maximum growth index is on U5 (0.28).

In addition, EI and GI for F4 revealed thickening on the hangingwall strata of U6, U7 and U9 and thinning on U4, U5 and U8 (Figs. 9 and 10). Most of the units have negative GI values. On U6, the growth index approaches 0.5 justifying the reverse drag observed on the seismic sections (Figs. 6 and 10). The reverse drag on U5 is the reason for the minimum GI of - 2 estimated along F3. For F5, there is strata thickening on U5b, U6, and U9 (Fig. 9 and 10) with no variation in thickness of the hanging-wall of U2 (EI = GI = 0). The maximum expansion and growth indices measured on U5b along F5 are 1.1 and 0.3, respectively. F6 does not show any thickness variation on U4, U5a and U6. The maximum EI of 1.4 and GI of 0.3 were recorded on U5b (Figs. 9 and 10).

4.4 Interpreted high-amplitude anomalies (HAA) and vertically focused fluid-flow

'Soft reflections' anomalies in this work are thought to be related to subsurface fluid accumulations and were mapped based on the following criteria; (1) their high amplitude values, (2) opposite polarity to the seabed reflectors, and (3) conformity to the background reflectors (Alves et al., 2015; Calvès et al., 2008). Nine soft reflections were interpreted and are shown in Figs. 11 and 12. The anomalies are spatially dominant in the eastern and western parts of Unit 9. Most of the anomalies (A1, A2, A3, A6, A7, A8) occur approximately at the same stratigraphic level within the Torsk Formation (600 to 700 ms TWTT) while anomalies A4 and A5 are mapped within the Kveite/Kviting Formations (Fig. 12). The geometry and character of each of the anomalies are summarized in Table 1.

Relative to the major faults, most of the soft reflections are located on the hanging-wall section of the major faults (Fig. 13). In addition, the seabed fluid-flow features line up along the upper tips of some of the faults. Most of the observed pockmarks and buried pockmarks lie over the fault tips (Fig. 14). The seabed pockmarks are not restricted to the upper tips of the major faults only but also found close to the shallow and intermediate faults. Several glacial plough marks or burrows are also noted on the seabed. These structures show strong interaction with some of the pockmarks (Figs. 14a and 14c)

Evidence of vertically focused fluid flow in the study area include gas chimneys (Fig. 15). Three major gas chimneys are interpreted from the chaos seismic section. The chimneys were later isolated from the seismic volume using geobody extraction (Fig. 15). Geometrically, they include tabular-shaped (Chimney 1), cone-shaped (Chimney 2) and a Christmas tree structure (Chimney 3) (Fig. 15). The gas chimneys extend from about 2900 ms TWTT (~3 km). They have area coverage of about 12 km^2, 60 km^2 and 17 km^2, for Chimney 1 to Chimney 3. Some of the high-amplitude anomalies or soft reflections are found at the upper section of the major gas chimneys (e.g., A1, A6 and A8).

5.0 Discussion

5.1 History and growth of faults in the study area

Faults in the study area are normal dip-slip faults with both reverse and normal drag on their hanging-wall sections. The observed fault drag implies mechanical heterogeneity and complex evolution of the faults. In addition, the displacement plots in Section 4.3 provide useful insights into fault nucleation, reactivation and interactions through time. These plots revealed complex fault segmentation along the strike and dip of the faults (Figs. 7 and 8). T-z plots for the major faults show that all the faults have multiple segments (Fig. 7). For example, F4 has two segments, one from H8 to H7 and the other from H7 to H4. This pattern is the same for the other faults. Similarly, the t-x profile across H4 to H6 varies for each of the faults suggesting variable lateral segmentation along strike and across different stratigraphic intervals (Fig. 8). Hence, the major faults in the study area have complex lateral and vertical segmentation.

Based on the t-z profiles, the faults are grouped into three types: (a) Those characterized by a centrally located point of maximum displacement (d_{max}) and general decrease in gradient at their upper and lower tips e.g., F1, F2 and F5. (b) profiles with an upward increase in gradient e.g., F3 and F4, and (c) profiles characterized by two points of d_{max} where the upper tip displays a gradual decrease in fault throw e.g., F6. Concerning fault nucleation, all the faults have their point of maximum displacement at horizon H5 except F6. Hence, if the point of nucleation coincides with the point of maximum displacement, then most of the deep-seated faults are nucleated in the reservoir zone. However, the points of maximum displacement can vary as a function of mechanical heterogeneity, fault segmentation, and linkage (*cf.* Cowie, 1998; Peacock and Sanderson, 1991).

As for the mode of fault propagation, a multiple mode of fault propagation including radial propagation and syn-sedimentary activity is inferred for the faults from Figs. 7 to 10. For example, F1 provides evidence of syn-sedimentary activity from horizons H4 to H6 while the rest of the profile has a blind propagation character (Fig. 7a). The lower part of F1, F2 and F5, and the upper part of F4 exhibit syn-sedimentary fault growth (Fig. 7). Only F3 and F6 show that they developed solely through blind propagation of their tips as they have elliptical to sub-elliptical profiles with a centrally located d_{max} (Fig. 7). In terms of their interaction with sedimentation, the growth and expansion indices reveal that some of the major faults are syn-sedimentary at their upper most sections while others did not interact with a free surface during their growth (Fig. 9). Hence, the majority of the faults have expansion indices of > 0.1 suggesting that strata growth on their hanging-wall section exceeds the footwall section. F1 has a t-z profile with both syn-sedimentary and blind character. At horizons H4 to H6, the faults propagated by syn-sedimentary activity, F1 was also formed coevally with sedimentation but was never exposed above any of the stratigraphic units during its growth. Hence, the majority of the deep-seated faults were formed by coalescence of initial isolated fault strands which were later reactivated along the dip direction i.e. dip-linkage.

Evidence of reactivation by dip-linkage is indicated as displacement minima along the t-z profiles of F1, F4 and F6 (Figs. 7a, 7d, and 7f). These points of displacement minima indicate that the upper and the lower segments of F1, F4 and F6 have been linked along dip over time. Fault reactivation by dip linkage was only inferred for the deep-seated faults. In the study area we propose that the non-reactivated faults include: (1) the shallow faults and (2) intermediate faults terminated in Unit 5 within the Upper Cretaceous to younger formations (Fig. 5). This is an indication that fault reactivation was dominant prior to the Late Cretaceous presumably at the end of the Late Jurassic. Evidence of active tectonics during the Late Jurassic is signified by Faults F1 and F2 by the significant change in their t-z profiles at horizon H6 (Upper Jurassic). The displacement minima or dip-linkage is noted at horizon H7, which is Lower Cretaceous. In addition to this, minor evidence of fault reactivation during Paleocene times is shown by F1 at the base of the Torsk Formation. Therefore, three episodes of fault reactivation in Late Jurassic, Early Cretaceous and Early Paleocene times are proposed for the study area. The presence of the shallow faults above Unit 8 implies that they were probably formed after the main phases of fault reactivation. Reactivated faults in this study have greater throw values than their non-reactivated counterparts. An average throw value of 100 ms TWTT (100 m) was estimated for the reactivated faults.

Three modes of fault reactivation are suggested for the deep-seated faults (a) upward reactivation of pre-existing (b) dip-linkage and (c) strike linkage. Upward reactivation of pre-existing faults is indicated by the reverse drag observed on some of the faults. Fig. 6 shows that the fault between F6 and F2 has opposing drags from H4 to H5. An indication that normal drag was developed at the level of H4 while reversed drag occurred in response to fault reactivation between H5 and H6. Reactivation by dip-linkage occurs when initially isolated fault sets coalesced into a single coherent structure by accumulating displacement over time. Dip-linkage is marked on t-z profiles by displacement minima connecting separate segments of a fault (*cf.* Mansfield and Cartwright, 1996; Omosanya and Alves, 2014). Similarly, reactivation of fault by strike-linkage occurs when interact and link along strike. T-x plots for F3, F4 and F6 show consistent skewness towards particular directions. On the other hand, the profiles for F1, F2 and F5 are only consistent at the upper horizons i.e., on H5 and H6. T-x for F5 is skewed towards the left at H4 and H6 and later to the right on H6. Based on this asymmetry or variability of the t-x profiles across different stratigraphic levels, we conclude that these faults were formed due to along-strike reactivation or linkage. At different levels, the individual faults would be characterised by overlapping fault segments, which interact and coalesce into a single fault along strike over time. In map view, these faults will show two segments in different directions from the lower to the upper parts while in seismic sections they would appear as single faults.

5.2 Implications of fault growth and reactivation for hydrocarbon migration

The timing of fault activity has direct implications on hydrocarbon migration in the study area. Different indicators are proposed as evidence that the deep-seated faults are leaking. The first piece of evidence is the spatial proximity of the soft reflections (HAAs) with the major faults (Fig. 13). It is shown that the hydrocarbon-related anomalies are located on and are intersected by the major faults. The second piece of evidence is the high throw values estimated for the major faults at the reservoir zone. High fracturing has led to leakage or migration of hydrocarbons from the reservoir rocks. These high throw or displacement values along the reservoir zone are thought to be related to the high degree of reactivation. Further evidence is the presence of gas chimneys that penetrate all the way upward from the Triassic (Snadd and Kobbe Formations) to the Torsk Formation.

As for fault reactivation, the drags interpreted on Unit 5 show that the fault zones are highly fractured and that majority of the reverse drags were developed during reactivation. The multiple fault segments noted on the displacement plots also point to a high degree of fracturation along the faults. Fault reactivation can mechanically fracture and brecciate fault zones creating secondary porosity, which can facilitate hydrocarbon spill from the reservoir. Since the soft reflections are intersected and segmented by the shallow faults, it implies that the fluid accumulations have migrated to their current stratigraphic position before the onset of the Late Paleocene to Eocene faulting. Based on this, the last episode of fluid migration from the source rock to the shallow subsurface accumulation is likely before the Paleocene-Eocene faulting. Here, the shallow fluid accumulations are unaffected by the Late Cretaceous faults as observed from seismic sections and RMS amplitude time slices. Therefore, it is suggested that the first phase of fluid migration was during the Late Jurassic. The second and third phases of fluid migration are linked to the Late Cretaceous and Paleocene fault reactivations. It is quite theoretical to constrain the degree of fluid migrated during each phase of fault reactivation. Nonetheless, the degree of fault reactivation during Late Cretaceous is relatively less, which in turn implies that the amount of hydrocarbons leaked or migrated during this period was probably less relative to Late Jurassic and Paleocene times.

Pockmarks and furrows/plough marks on the URU and seabed provide evidence that fluid-flow was active during the early stages of glaciation and is an ongoing process in the study area (Fig. 14). The URU corresponds to the base of the Quaternary deposit in the Barents Sea and it is recognized as an erosional boundary. The Quaternary unit is composed of glacigenic sediments deposited during the latest glaciation in the entire Barents Sea (Dalland et al., 1988). The URU separates the glacigenic sediments from deeper, non-glacial and well-bedded rocks in the study area. Based on the large number of pockmarks documented on the URU, a phase of fluid migration may have taken place before the last glacial maximum (LGM).

5.3 Source of hydrocarbons and migration pathways

The plumbing system and the conceptual model for hydrocarbon migration in the study area are presented in Figs. 15 and 16. The nine soft reflections have reversed or opposite polarities to the seabed, negative high amplitudes, and can be classified further based on their conformability with their background structural reflectors. The first group of anomalies is structurally conformable and the anomalies are aligned in the same direction as the background reflectors, e.g., A4, A5 and A9 (Fig. 12). Based on their flatness, these anomalies are difficult to interpret as flat spots especially when the seismic volume is interpreted in the time domain. Alternatively, their flat geometry may imply that they are static fluid accumulations. In addition, this group of anomalies is not spatially related to the major faults and is controlled largely by the stratigraphic or geomorphic structures. Anomalies A4 and A5 are hosted in Unit 8 while A9 is hosted in Unit 4. The second group of soft reflections (A1, A2, A3, A6, A7 and A8) is structurally unconformable to the background reflectors and is also interpreted as fluid accumulations. They are hosted in Unit 9 and spatially located on the upper parts of the major faults.

Apart from the soft reflections, other fluid flow features interpreted in the study area include pockmarks and gas chimneys (Figs. 14 and 15). The source area for hydrocarbons in the study area may include; (a) Triassic formations, since the gas chimneys extend from Unit 4 upward to the Eocene, Unit 9, and (b) Jurassic intervals through which the deep-seated faults intersected (Fig. 13). Figure 15 indicates that the gas chimneys emerged from H6 and the units below it. The areal extent of acoustic masking associated with the chimneys increases upward from the reservoir zone indicating that more hydrocarbons were leaked from the reservoir through the chimneys. The geometry of the extracted chimneys also point to the likely mode of fluid leakage. Chimney 3 with a Christmas-tree geometry signifies episodic fluid leakage where the fluid were leaked at different times. The other chimneys on the other hand show evidence of regular and consistent leakage of fluid in the study area.

Faults unlike chimneys can act as either barriers or conduits for fluids depending on the nature of the fault. Brecciation and fracturing can enhance porosity, permeability, and fluid migration pathways across fault zones. Conversely, fault-related diagenesis, clay smearing can block the permeability of the fault zone in which case it will act as a subsurface fluid-flow barrier (*cf*. Ferrill and Morris, 2001; Yielding et al., 1997). Since most of the hydrocarbon-related anomalies are located on the hanging-wall side of the deep-seated faults and the fact that the throws estimated along most of the faults are more than 30 ms (30 m), it is hypothesized that the deep-seated faults in the study area were initially barriers to hydrocarbon migration. However, the sealing integrity of the faults was presumably compromised during the different phases of fault reactivation. Therefore, the present-day configurations of the faults on the contrary suggest they are the primary conduits for hydrocarbon migration in the study area. The degree of fault segmentation and reactivation provides proof for fluid leakage and transmission through the faults. Hence, the mechanism for hydrocarbon leakage in the Snøhvit Gas Field is through tectonic fracturing. At shallow levels or during the proposed fourth episode of fluid migration, hydro-fracturing is thought to be enhanced by uplift and erosion which are the main processes driving fluid migration during the glaciation periods (see also Chand et al., 2014; Ostanin et al., 2013).

6.0 Conclusions

- Six major deep-seated faults extending from the Upper Carboniferous to Eocene rocks are linked with hydrocarbon migration in the Snøhvit Gas Field, Hammerfest Basin. These faults have their maximum throws at the Middle Jurassic reservoir interval. The throw and displacement profiles of the major faults reveal polycyclic fault history involving both blind propagation and syn-sedimentary activity.
- The expansion indices of the deep-seated major faults are consistent with displacement analysis and show strata thickening along the hanging-wall side of the reservoir zone. The growth indices suggest that the major faults interacted with the free surface during their evolution, except for F6, which is a blind fault.

- The faults have complex lateral and vertical segmentation or linkage. Most of the major faults interacted and linked along the strike direction. Fault reactivation was dominantly through dip-linkage. Three phases of fault reactivation in the Late Jurassic, Early Cretaceous and Paleocene-Early Eocene are proposed for the faults.
- Nine hydrocarbon-related anomalies are mapped and multiple seismic attribute analysis was employed. The anomalies are spatially located in the upper parts of the major faults and on top of the gas chimneys. Six of these hydrocarbon anomalies are unconformable with structural reflectors and are interpreted as static fluid accumulations. The structurally conformable soft reflections are stratigraphically controlled and have no spatial relationship with the deep-seated faults.
- The major deep-seated faults are the main hydrocarbon migration pathways from the Triassic source rocks and the Jurassic reservoirs; further leakage to the seabed was through the younger Paleocene to Early Eocene faults. The main driving and trigger mechanisms for fluid-flow in the study area are tectonic fracturing and/or hydro-fracturing. Fluids or hydrocarbons migrated laterally and vertically from Jurassic and Triassic units into shallow levels. Fluid-flow is an active process in the Snøhvit Gas Field as is evidenced by the presence of present-day seabed pockmarks and furrows.

Acknowledgement

We appreciate the Norwegian Petroleum Directorate (NPD) and IPT NTNU for access to the seismic and well data used in this research and Schlumberger for provision of Petrel® for seismic interpretation. The participation of Kamal'deen Omosanya and Ståle Johansen in this research is sponsored by the ARCEx project (Research Centre for Arctic Petroleum Exploration) which is funded by the Research Council of Norway (grant number 228107) together with 10 academic and 9 industry partners.

References

Alves, T.M., Omosanya, K.O., Gowling, P., 2015. Volume rendering of enigmatic high-amplitude anomalies in southeast Brazil: A workflow to distinguish lithologic features from fluid accumulations. Interpretation 3, 1–14.

Andreassen, K., Laberg, J.S., Vorren, T.O., 2008. Seafloor geomorphology of the SW Barents Sea and its glaci-dynamic implications. Geomorphology 97, 157–177. doi:10.1016/j.geomorph.2007.02.050

Arvo, J., 2014. Relationship between fluid leakage and faulting along the western and northern margin of the Hammerfest Basin (MSc). The Arctic University of Norway, Tromsø.

Barrère, C., Ebbing, J., Gernigon, L., 2009. Offshore prolongation of Caledonian structures and basement characterisation in the western Barents Sea from geophysical modelling. Prog. Underst. Sediment. Basins 470, 71–88. doi:10.1016/j.tecto.2008.07.012

Berglund, L.T., Augustson, J., Færseth, R., Gjelberg, J., Ramberg-Moe, H., 1986. The evolution of the Hammerfest Basin. Habitat Hydrocarb. Nor. Cont. Shelf 319–338.

Breivik, A.J., Mjelde, R., Grogan, P., Shimamura, H., Murai, Y., Nishimura, Y., Kuwano, A., 2002. A possible Caledonide arm through the Barents Sea imaged by OBS data. Tectonophysics 355, 67–97.

Brown, A.., 2004. Interpretation of Three-Dimensional Seismic Data, Sixth. ed. American Association of Petroleum Geologists (AAPG), Tulsa.

Calvès, G., Huuse, M., Schwab, A., Clift, P., 2008. Three-dimensional seismic analysis of high-amplitude anomalies in the shallow subsurface of the Northern Indus Fan: Sedimentary and/or fluid origin. J. Geophys. Res. 113, B11103–B11103. doi:10.1029/2008JB005666

Cavanagh, A.J., Di Primio, R., Scheck-Wenderoth, M., Horsfield, B., 2006. Severity and timing of Cenozoic exhumation in the Southwestern Barents Sea. J. Geol. Soc. 163, 761–774.

Chand, S., Knies, J., Baranwal, S., Jensen, H., Klug, M., 2014. Structural and stratigraphic controls on subsurface fluid flow at the Veslemøy High, SW Barents Sea. Mar. Pet. Geol. 57, 494–508. doi:10.1016/j.marpetgeo.2014.06.004

Chand, S., Mienert, J., Andreassen, K., Knies, J., Plassen, L., Fotland, B., 2008. Gas hydrate stability zone modelling in areas of salt tectonics and pockmarks of the Barents Sea suggests an active hydrocarbon venting system. Mar. Pet. Geol. 25, 625–636. doi:10.1016/j.marpetgeo.2007.10.006

Chand, S., Thorsnes, T., Rise, L., Brunstad, H., Stoddart, D., Bøe, R., Lågstad, P., Svolsbru, T., 2012. Multiple episodes of fluid flow in the SW Barents Sea (Loppa High) evidenced by gas flares, pockmarks and gas hydrate accumulation. Earth Planet. Sci. Lett. 331–332, 305–314. doi:10.1016/j.epsl.2012.03.021

Cowie, P.., 1998. Normal fault growth in three-dimensions in continental and oceanic crust, in Faulting and Magmatism at Mid-Ocean Ridges: Geophys. Monogr. 106, 325–348.

Doré, A.G., Jensen, L.N., 1996. The impact of late Cenozoic uplift and erosion on hydrocarbon exploration: offshore Norway and some other uplifted basins. Impact Glaciat. Basin Evol. Data Models Nor. Margin Adjac. Areas 12, 415–436. doi:10.1016/0921-8181(95)00031-3

Faleide, J.I., Gudlaugsson, S.T., Jacquart, G., 1984. Evolution of the western Barents Sea. Mar. Pet. Geol. 1, 123–150. doi:10.1016/0264-8172(84)90082-5

Faleide, J.I., Tsikalas, F., Breivik, A.J., Mjelde, R., Ritzmann, O., Engen, Ø., Wilsom, J., Eldholm, O., 2008. Structure and evolution of the continental margin off Norway and the Barents Sea. Episodes 31, 82–91.

Faleide, J.I., Vågnes, E., Gudlaugsson, S.T., 1993. Late Mesozoic-Cenozoic evolution of the south-western Barents Sea in a regional rift-shear tectonic setting. Mar. Pet. Geol. 10, 186–214. doi:10.1016/0264-8172(93)90104-Z

Ferrill, D.A., Morris, A.P., 2001. Displacement gradient and deformation in normal fault systems. J. Struct. Geol. 23, 619–638. doi:10.1016/S0191-8141(00)00139-5

Gabrielsen, R.H., Færseth, R.B., Jensen, L.N., Kalheim, J.E., Riis, F., 1990. Structural elements of the Norwegian Continental Shelf. Part 1: The Barents Sea region. NPD-Bull. No 6 33 PP.

Gay, A., Takano, Y., Gilhooly Iii, W.P., Berndt, C., Heeschen, K., Suzuki, N., Saegusa, S., Nakagawa, F., Tsunogai, U., Jiang, S.Y., 2011. Geophysical and geochemical evidence of large scale fluid flow within shallow sediments in the eastern Gulf of Mexico, offshore Louisiana. Geofluids 11, 34–47.

Gee, D.G., Fossen, H., Henriksen, N., Higgins, A.K., 2008. From the early Paleozoic platforms of Baltica and Laurentia to the Caledonide Orogen of Scandinavia and Greenland. Episodes 31, 44.

Gernigon, L., Brönner, M., Roberts, D., Olesen, O., Nasuti, A., Yamasaki, T., 2014. Crustal and basin evolution of the Southwestern Barents Sea: from Caledonian orogeny to continental breakup. Tectonics 33, 347–373.

Glørstad-Clark, E., Faleide, J.I., Lundschien, B.A., Nystuen, J.P., 2010. Triassic seismic sequence stratigraphy and paleogeography of the western Barents Sea area. Mar. Pet. Geol. 27, 1448–1475. doi:10.1016/j.marpetgeo.2010.02.008

Gudlaugsson, S.T., Faleide, J.I., Johansen, S.E., Breivik, A.J., 1998. Late Palaeozoic structural development of the south-western Barents Sea. Mar. Pet. Geol. 15, 73–102.

Heggland, R., 1998. Gas seepage as an indicator of deeper prospective reservoirs. A study based on exploration 3D seismic data. Mar. Pet. Geol. 15, 1–9.

Henriksen, E., Bjørnseth, H.M., Hals, T.K., Heide, T., Kiryukhina, T., Kløvjan, O.S., Larssen, G.B., Ryseth, A.E., Rønning, K., Sollid, K., 2011. Uplift and erosion of the greater Barents Sea: impact on prospectivity and petroleum systems. Geol. Soc. Lond. Mem. 35, 271–281.

Hongxing, G., Anderson, J.K., 2007. Fault throw profile and kinematics of Normal fault: conceptual models and geologic examples. Geol J China Univ 13, 75–88.

Hovland, M., Judd, A.., 1988. Seabed Pockmarks and Seepages. Impact on Geology, Biology and the Marine Environment. Graham and Trotman Ltd, London.

Johansen, S.E., Ostisty, B.K., Birkeland, Ø., Fedorovsky, Y.F., Martirosjan, V.N., Christensen, O.B., Cheredeev, S.I., Ignatenko, E.A., Margulis, L.S., 1992. Hydrocarbon potential in the Barents Sea region: play distribution and potential. Arct. Geol. Pet. Potential Nor. Pet. Soc. NPF Spec. Publ. 2, 273–320.

Klitzke, P., Faleide, J.I., Scheck-Wenderoth, M., Sippel, J., 2014. A lithosphere-scale structural model of the Barents Sea and Kara Sea region. Solid Earth Discuss. 6, 1579–1624.

Knutsen, S.-M., Vorren, T.O., 1991. Early Cenozoic sedimentation in the Hammerfest Basin. Mar. Geol. 101, 31–48.

Løseth, H., Gading, M., Wensaas, L., 2009. Hydrocarbon leakage interpreted on seismic data. Mar. Pet. Geol. 26, 1304–1319. doi:10.1016/j.marpetgeo.2008.09.008

Mansfield, C.S., Cartwright, J.A., 1996. High resolution fault displacement mapping from three-dimensional seismic data: evidence for dip linkage during fault growth. J. Struct. Geol. 18, 249–263.

Mienert, J., Vanneste, M., Bünz, S., Andreassen, K., Haflidason, H., Sejrup, H.P., 2005. Ocean warming and gas hydrate stability on the mid-Norwegian margin at the Storegga Slide. Mar. Pet. Geol. 22, 233–244.

Muraoka, H., Kamata, H., 1983. Displacement distribution along minor fault traces. J. Struct. Geol. 5, 483–495.

Ohm, S.E., Karlsen, D.A., Austin, T.J.F., 2008. Geochemically driven exploration models in uplifted areas: Example from the Norwegian Barents Sea. AAPG Bull. 92, 1191–1223.

Omosanya, K., O., Alves, T.M., 2014. Mass-transport deposits controlling fault propagation, reactivation and structural decoupling on continental margins (Espírito Santo Basin, SE Brazil). Tectonophysics 628, 158–171. doi:10.1016/j.tecto.2014.04.045

Ostanin, I., Anka, Z., di Primio, R., Bernal, A., 2013. Hydrocarbon plumbing systems above the Snøhvit gas field: structural control and implications for thermogenic methane leakage in the Hammerfest Basin, SW Barents Sea. Mar. Pet. Geol. 43, 127–146.

Ottesen, S., Folkestad, A., Gawthorpe, R., 2005. Tectono-stratigraphic development of the Hammerfest Basin (Northern Norway) during the Jurassic to Cretaceous. AAPG Annual Meeting. abstruct volume.

Peacock, D.C.., Sanderson, D.., 1991. Displacements, segment linkage and relay ramps in normal fault zones. J. Struct. Geol. 13, 721–733. doi:10.1016/0191-8141(91)90033-F

Pochat, S., Castelltort, S., Choblet, G., Van Den Driessche, J., 2009. High-resolution record of tectonic and sedimentary processes in growth strata. Mar. Pet. Geol. 26, 1350–1364. doi:10.1016/j.marpetgeo.2009.06.001

Reeve, M.T., Bell, R.E., Duffy, O.B., Jackson, C.A.L., Sansom, E., 2015. The growth of non-colinear normal fault systems; What can we learn from 3D seismic reflection data? J. Struct. Geol. 70, 141–155. doi:10.1016/j.jsg.2014.11.007

Ritzmann, O., Faleide, J.I., 2007. Caledonian basement of the western Barents Sea. Tectonics 26.

Rodrigues Duran, E., di Primio, R., Anka, Z., Stoddart, D., Horsfield, B., 2013. Petroleum system analysis of the Hammerfest Basin (Southwestern Barents Sea): Comparison of basin modelling and geochemical data. Org. Geochem. 63, 105–121. doi:10.1016/j.orggeochem.2013.07.011

Thorsen, C.E., 1963. Age of Growth Faulting in Southeast Louisiana. Gulf Coast Assoc. Geol. Soc. Trans. 13, 103–110.

Tvedt, A.B.M., Rotevatn, A., Jackson, C.A.-L., Fossen, H., Gawthorpe, R.L., 2013. Growth of normal faults in multilayer sequences: A 3D seismic case study from the Egersund Basin, Norwegian North Sea. J. Struct. Geol. 55, 1–20. doi:10.1016/j.jsg.2013.08.002

Vadakkepuliyambatta, S., Bünz, S., Mienert, J., Chand, S., 2013. Distribution of subsurface fluid-flow systems in the SW Barents Sea. Mar. Pet. Geol. 43, 208–221. doi:10.1016/j.marpetgeo.2013.02.007

Yielding, G., Freeman, B., Needham, D.T., 1997. Quantitative fault seal prediction. AAPG Bull. 81, 897–917.

Table 1: The geometry and orientation of the fluid-related high amplitude anomalies. Average length of the anomalies is twice of their width.

S/N	Length (m)	Width (m)	Aspect ratio	Shape	Elongation direction
A1	4252	2534	0.6	Spheroidal	NW-SE
A2	3615	1302	0.4	Oval	NW-SE
A3	3272	1248	0.4	Spheroidal	NW-SE
A4	3827	1953	0.5	Spherical	E-W
A5	2340	983	0.4	Sub-spherical	NW-SE
A6	7549	3648	0.5	Rectangular	N-S
A7	6942	4111	0.6	Oval and disseminated	NW-SE
A8	4942	2990	0.6	Oval	N-S
A9	681	362	0.5	Sub-angular	NW-SE

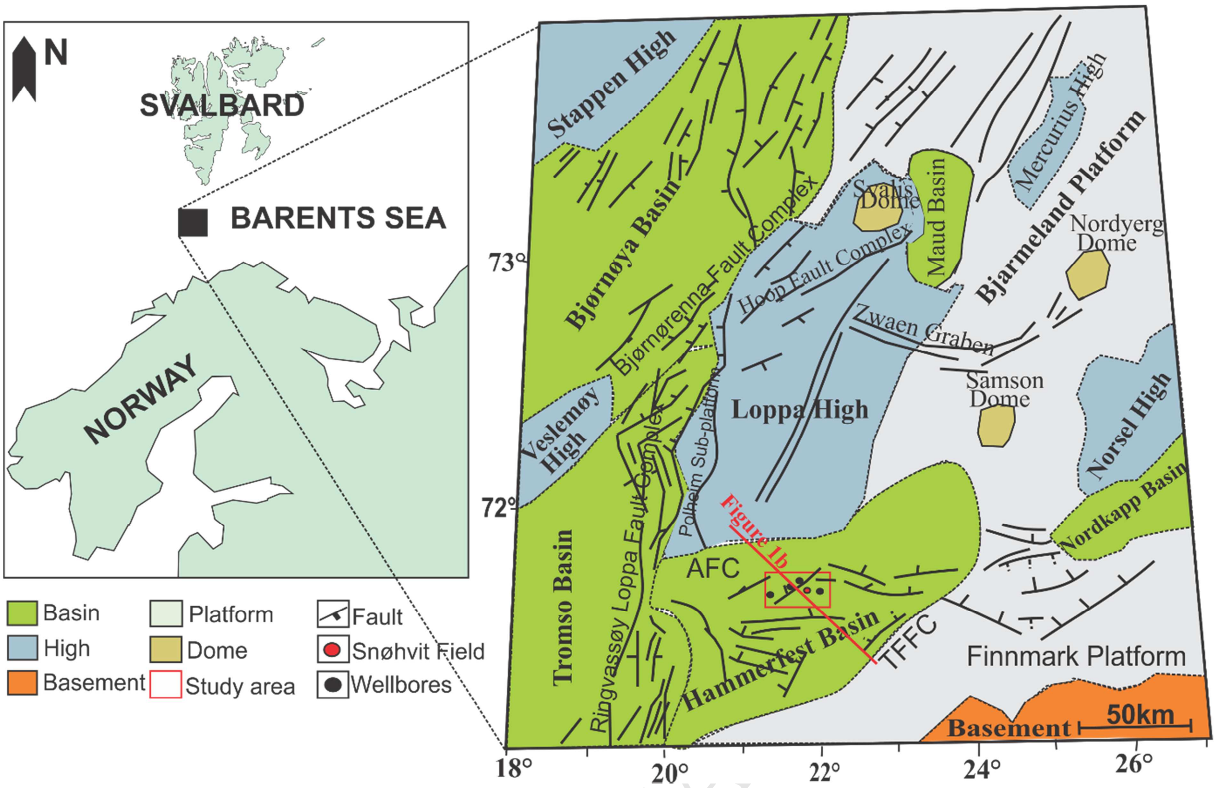

Fig. 1a: Location and tectonic map of the Southwestern Barents Sea and Snøhvit Gas Field (red rectangle) (modified from Gabrielsen et al.,1990). The study area is located in the Hammerfest Basin *N.B: The red line is the location of the geosection in Fig. 1b.*

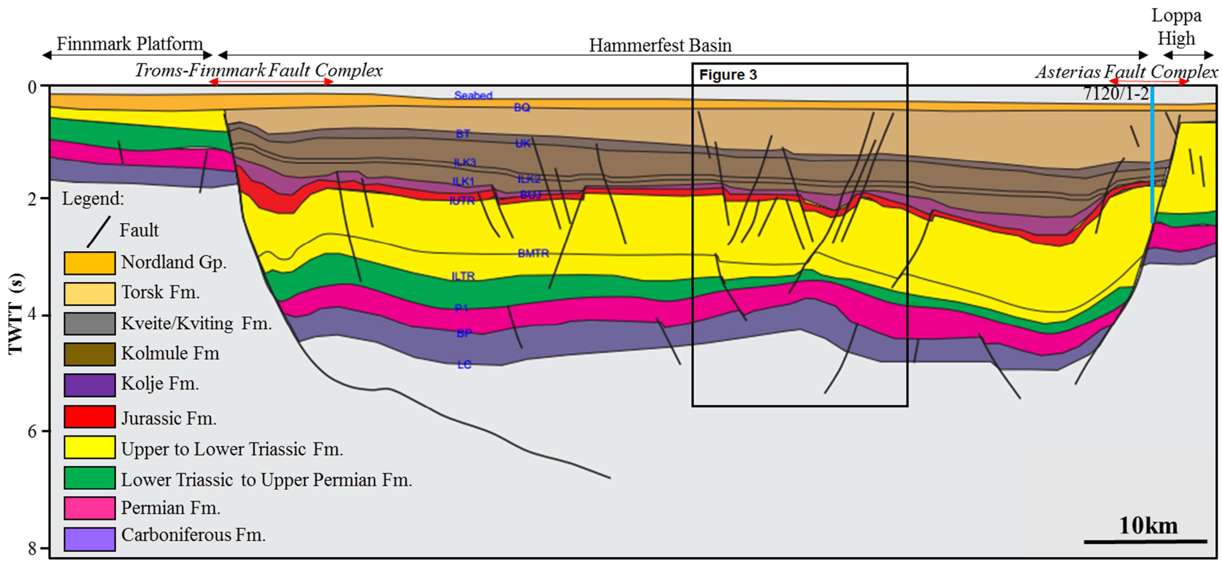

Fig. 1b: Geological cross section across the Hammerfest Basin, the Troms-Finnmark Platform, the Loppa High, the Troms-Finnmark Fault Complex and Asterias Fault Complex (Modified from Gabrielsen et al., 1990). *LC: Lower Carboniferous; BP: Base Permian; P1: top Permian; ILTR: Intra-lower Triassic; BMTR: Base Middle Triassic; IUTR: Intra-upper Triassic; BUJ: Base Upper Jurassic; ILK1, ILK1, ILK2 & ILK3 are Lower Cretaceous; UK: Upper Cretaceous; BT: Base Tertiary and BQ: Base of Quaternary.*

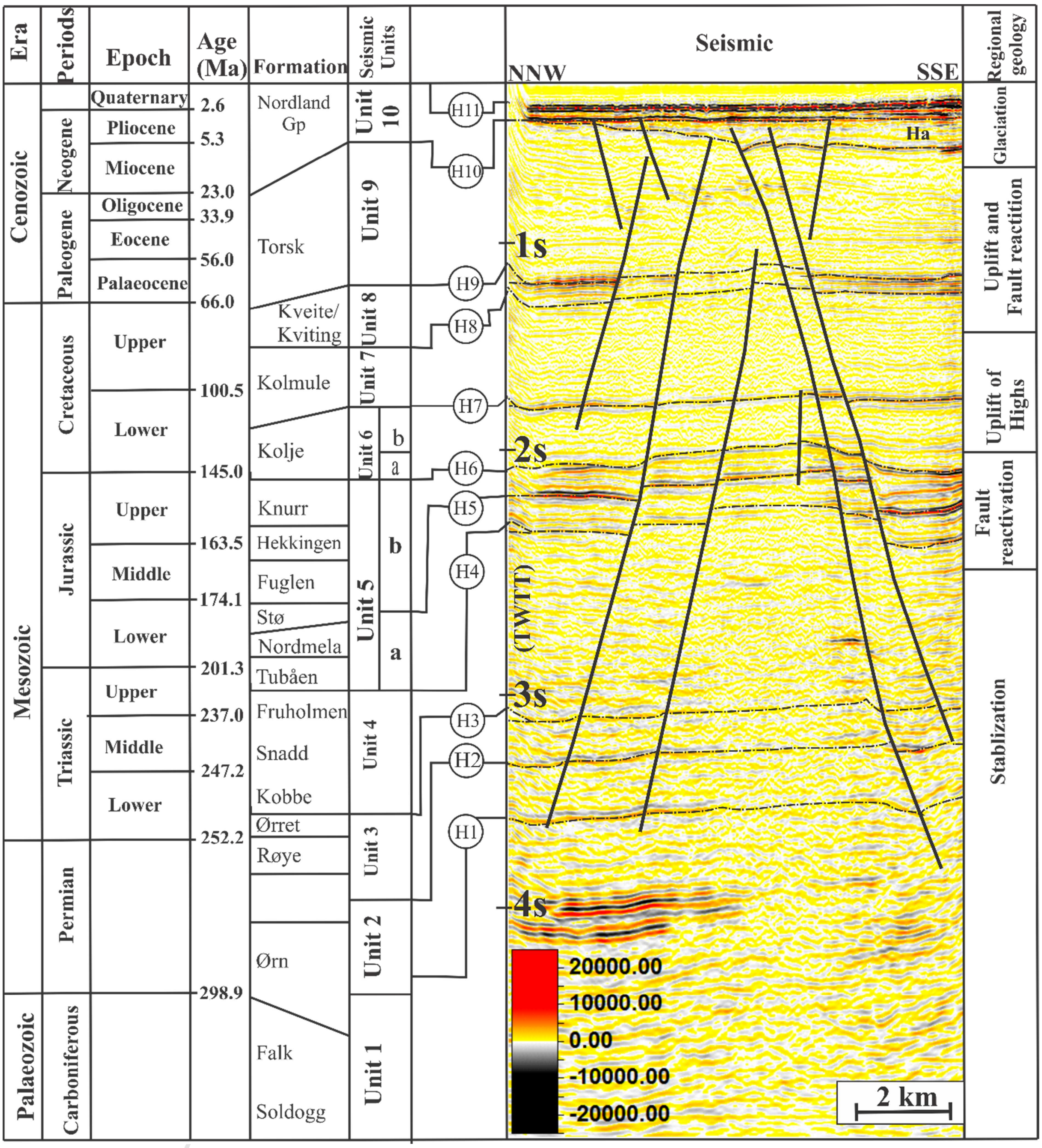

Fig. 2: Tectono-stratigraphic column of the Snøhvit Field showing the major units with their interpreted formation tops and the summarized tectonic history of the study area (modified from Ostanin et al., 2013). *See the location of seismic line in Fig.4. Ha is an arbitrary horizon that divides Unit 9 into U-9a and U-9b.*

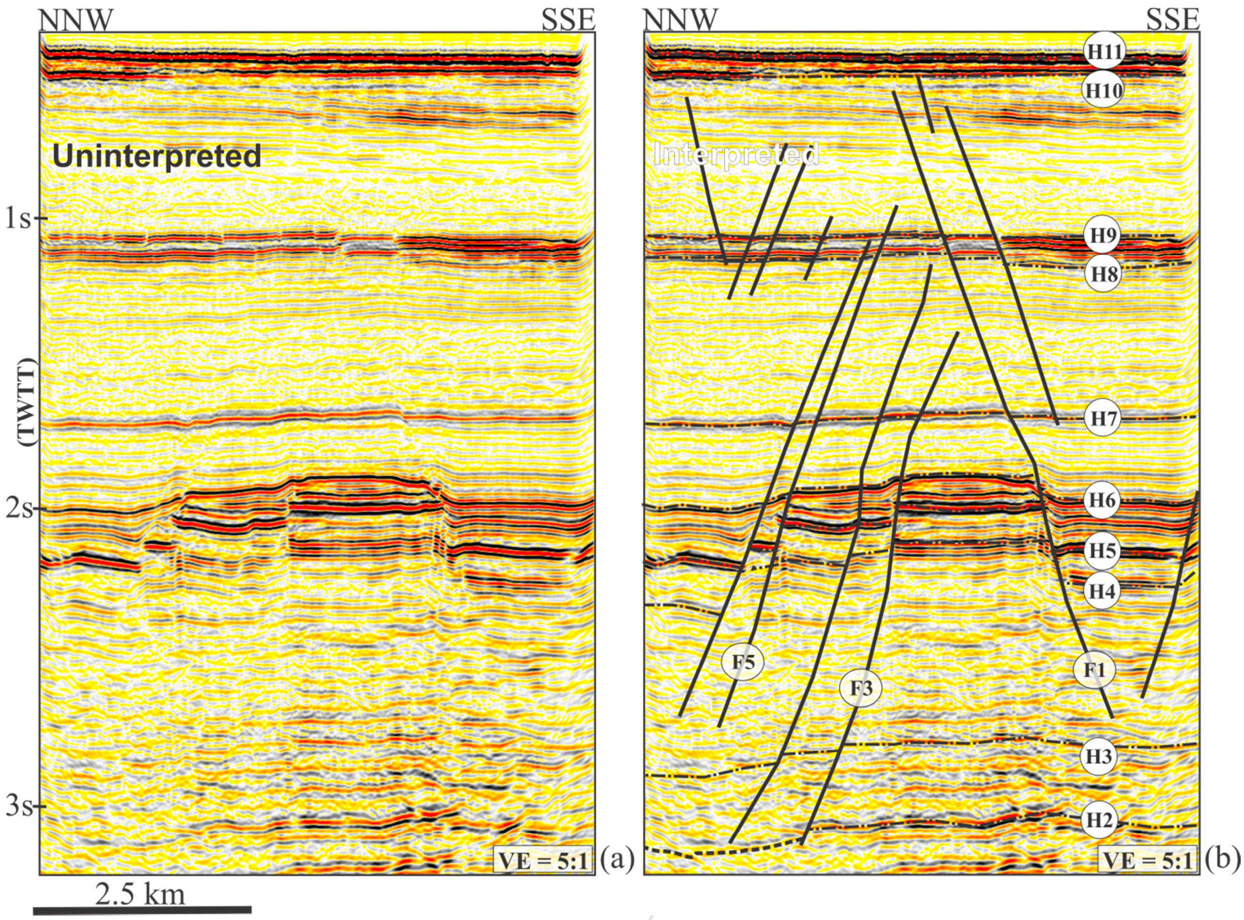

Fig. 3: (a) Uninterpreted and (b) interpreted seismic sections showing the some of the deep-seated faults interpreted in the work. Also shown in the Fig. is thickening along F1 and drag of sediments along the flank of the horst structure in the reservoir zone (H4 to H5).

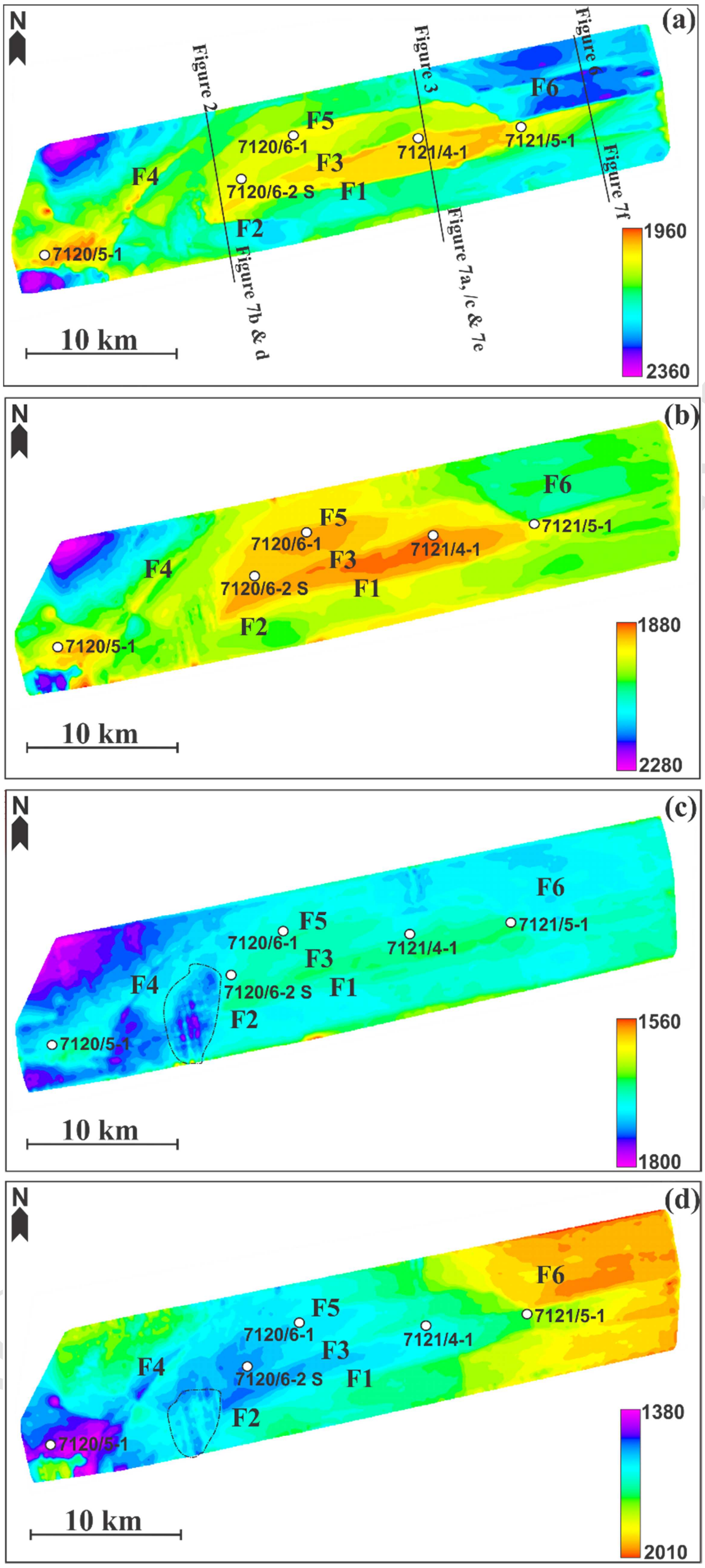

Fig. 4: (a) to (c) Isochron or structural maps for horizons H7, H6 and H5. The major faults offsetting these horizons are characterized by steep gradients. The black dotted-circle indicates areas of poor data quality linked to the presence of gas chimneys, (d) Isopach map across the reservoir zone showing the thickness variation on the downthrown sides of the major faults. *The locations of the five wells used in this study are also shown.*

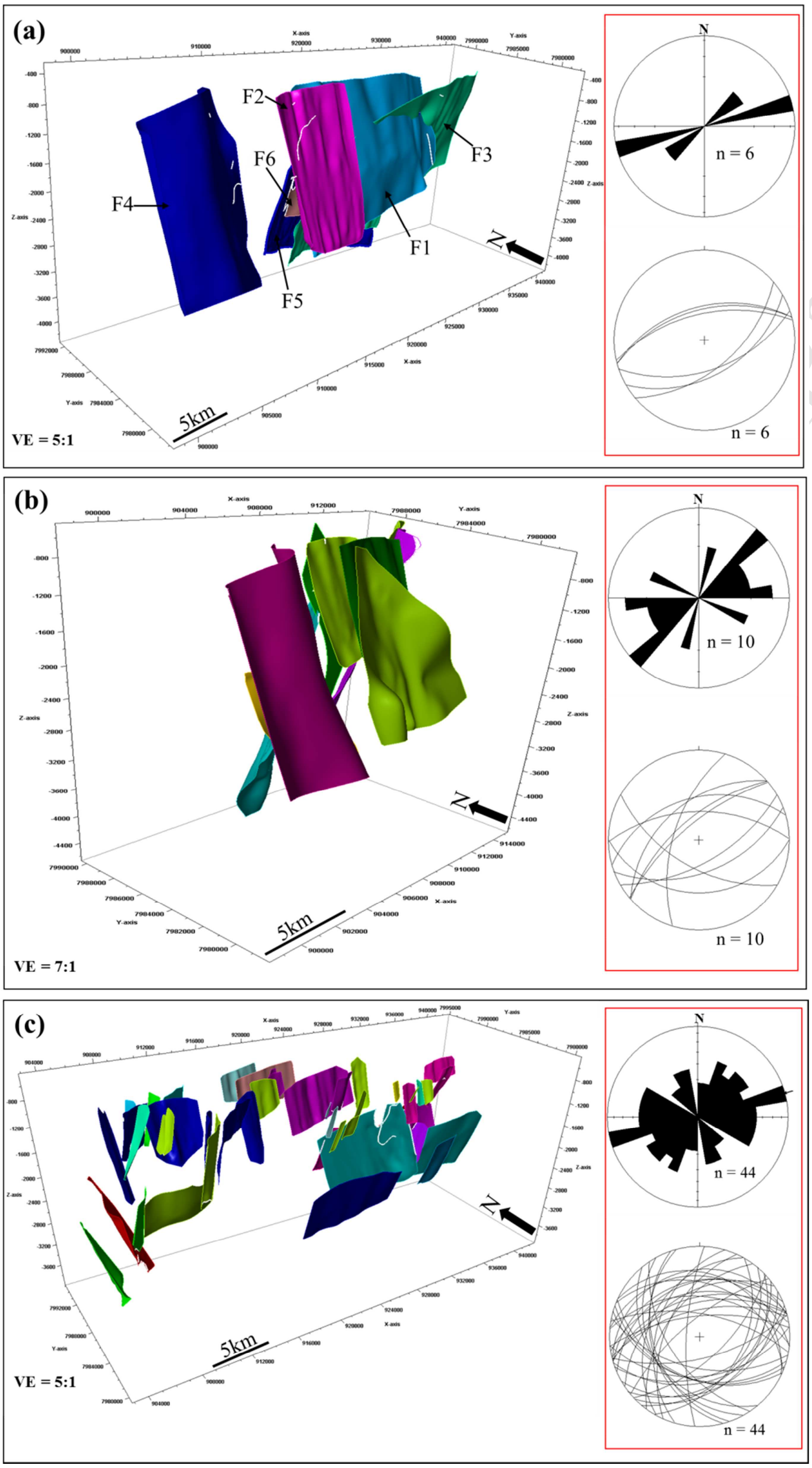

Fig. 5: Fault plane projections, rose diagrams, and equal area plots for (a) the six major faults discussed in the text. These faults are deep-seated faults and are extended to the Triassic, Permian and Carboniferous formations with their upper tips are terminated within Eocene sediments (b) Intermediate or Type B faults and (c) Shallow or Type C faults. The major faults and intermediate faults are mainly oriented in the ENE-WSE direction. Most of the minor faults are oriented E-W.

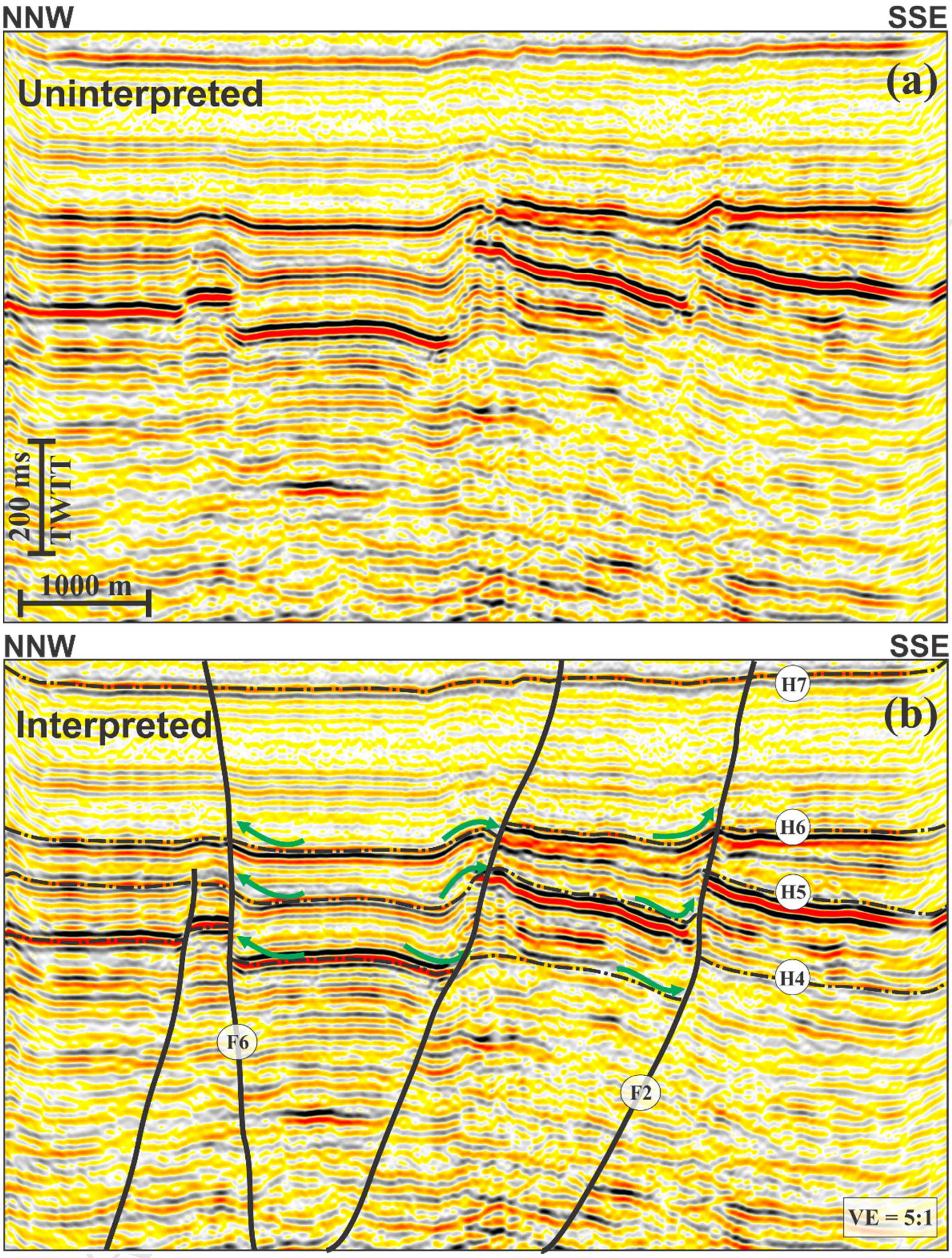

Fig. 6: (a) Uninterpreted and (b) Interpreted seismic section showing normal and reverse drag along the some of the interpreted faults. Fault drag is shown with green arrow. *See fig. 4 for location of the seismic sections.*

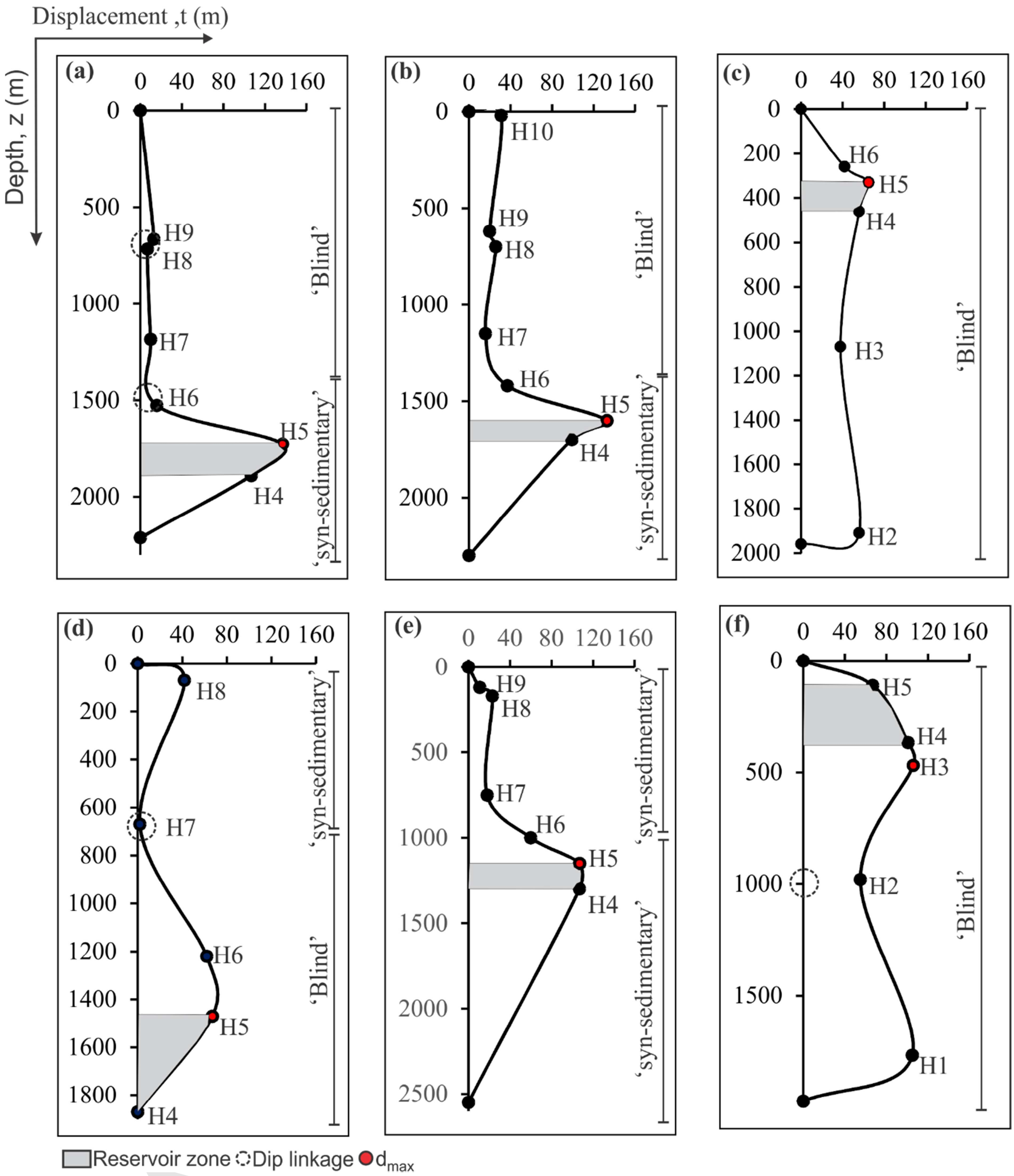

Fig. 7: Throw-depth (t-z) plots of the six major faults from (a) F1 to (f) F6, respectively. F1, F2, F3 and F5 have relatively steep gradients towards the lower part of the profiles with maximum throw estimated at H5. The throw minima noted on the t-z profile of F1, F4 and F5 are interpreted as evidence for dip-linkage. *N.B: the red dot indicates location of the maximum throw value.*

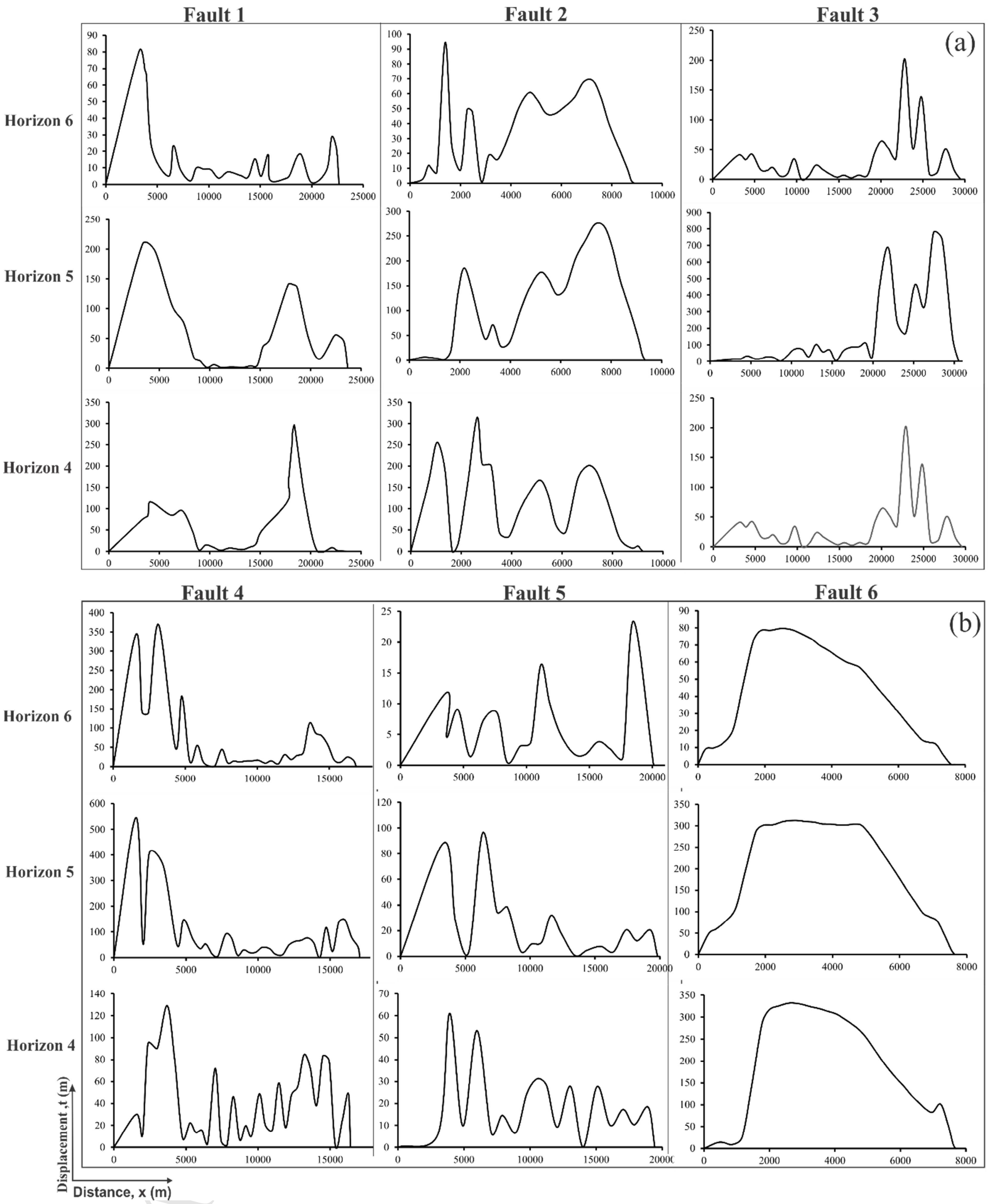

Fig. 8: Distance-displacement (t-x) plots of (a) Faults F1, F2 and F3 and (b) Faults F4, F5 and F6. The plots are made along horizons H4, H5 and H6, respectively. The t-x plots include m-type, c-type and skewed c-type profiles of Muraoka and Kamata, 1983. Only fault F6 is characterized by a simple profile signifying no segmentation or linkage of the fault along strike.

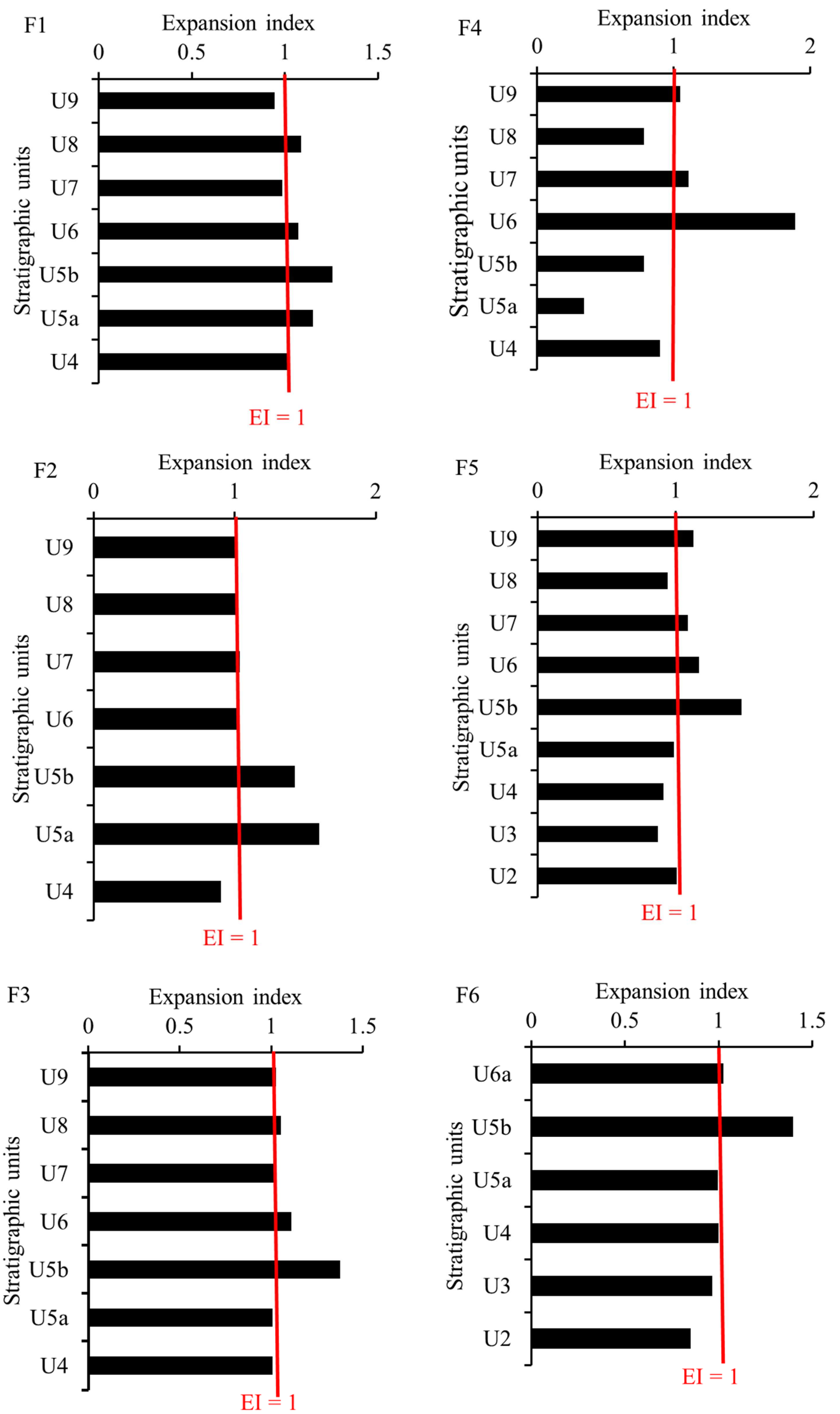

Fig. 9: The expansion indices (EI) for the major faults show variation in strata thickness across their hanging-wall and footwall sections. EI of > 1 implies thickening of strata in the hangingwall section while EI < 1 means thinning. *Expansion indices were estimated along the seismic section as Fig. 7*

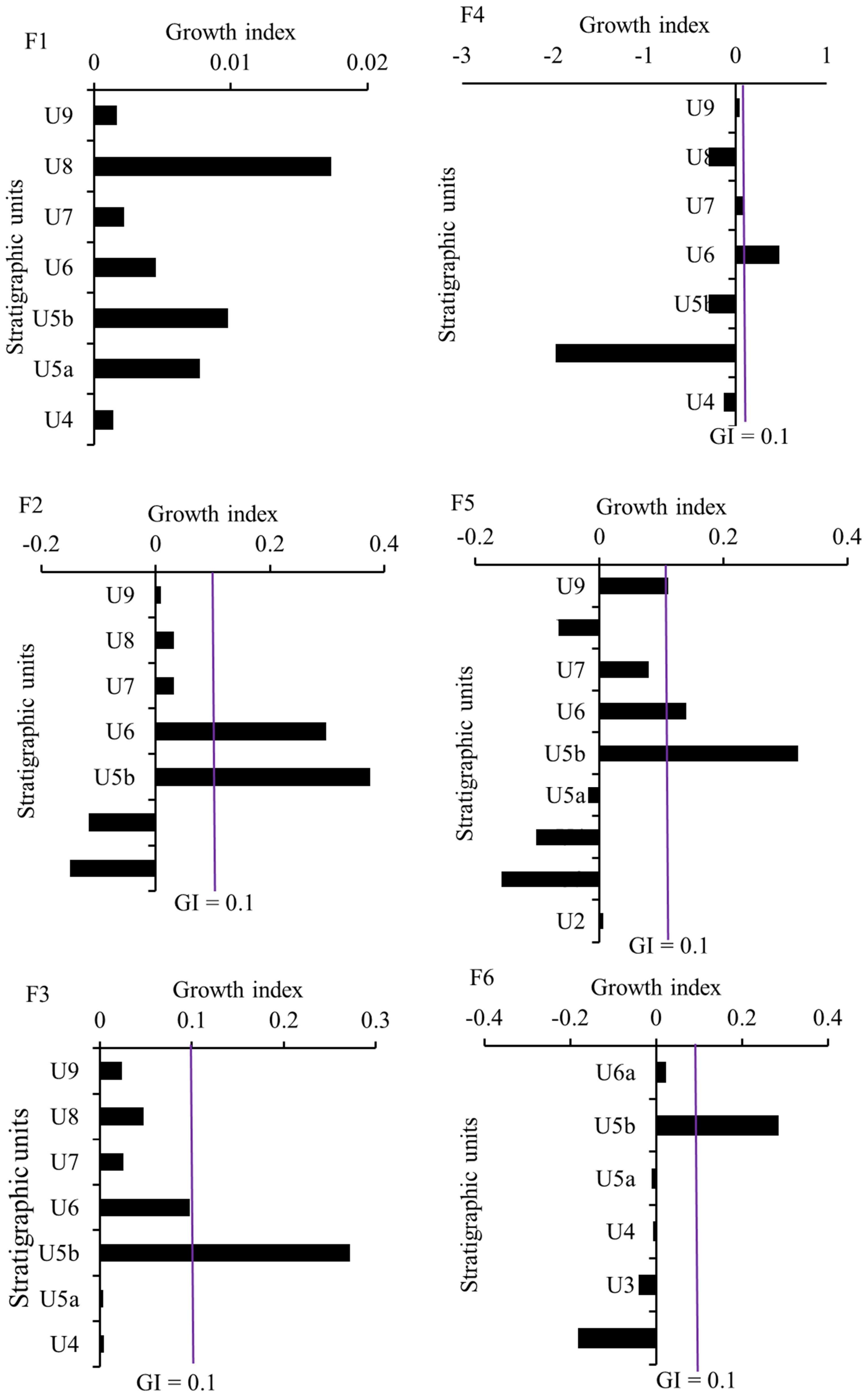

Fig. 10: The growth indices (GI) for the major faults. GI of > 1 implies the fault interacted with a free surface during its growth while GI < 1 means the faults was buried below a free surface i.e., blind fault. *Growth indices were estimated along the seismic section as Fig. 7.*

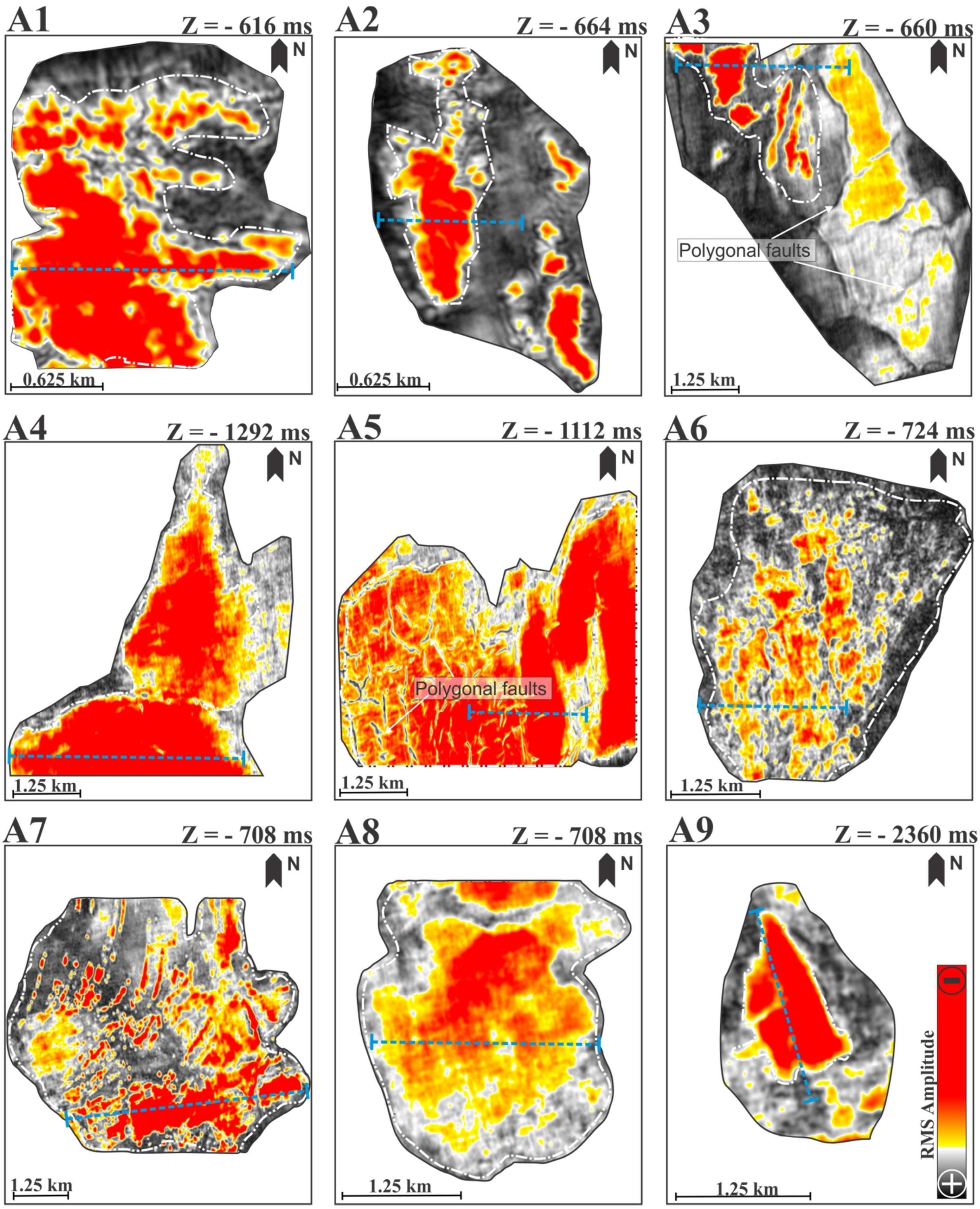

Fig. 11: On RMS amplitude time slices showing the soft reflection i.e., hydrocarbon related high ampltiude anomalies are revealed as brightening of negative amplitudes against the background positive amplitude value. The anomalies have variable geometries and are generally oblong to sub-circular in shape. N.B: *The blue dashed lines show the location of the corresponding seismic sections in Fig. 12.*

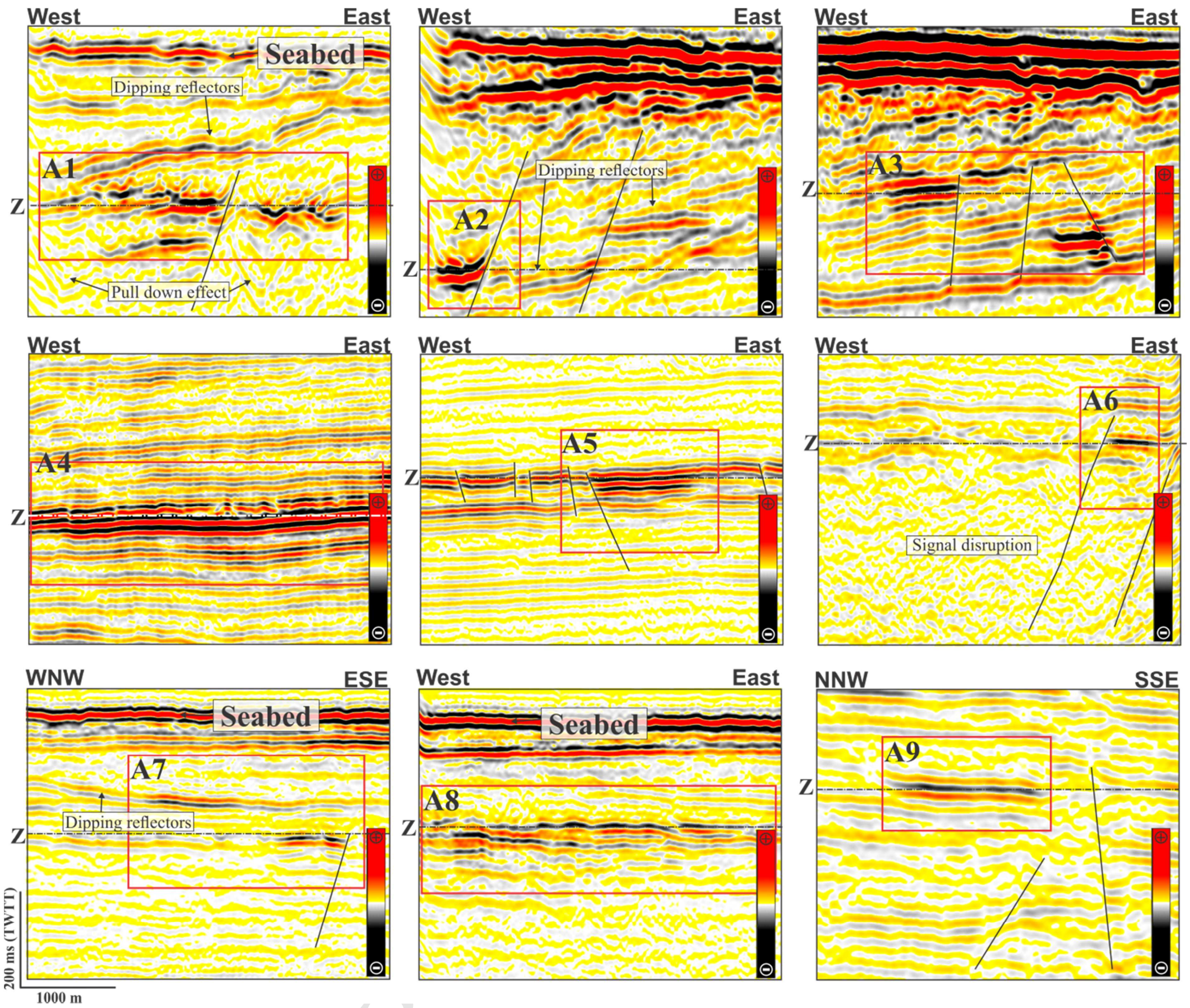

Fig. 12: Seismic sections showing the anomalies shown in Fig. 11. The soft reflections in the study area are localized brightening of negative amplitude with reserved polarity as compared to the seabed reflector. In addition, they show variable orientation to the background structural reflectors. N.B: *Location of RMS amplitude time slice is indicated as Z.*

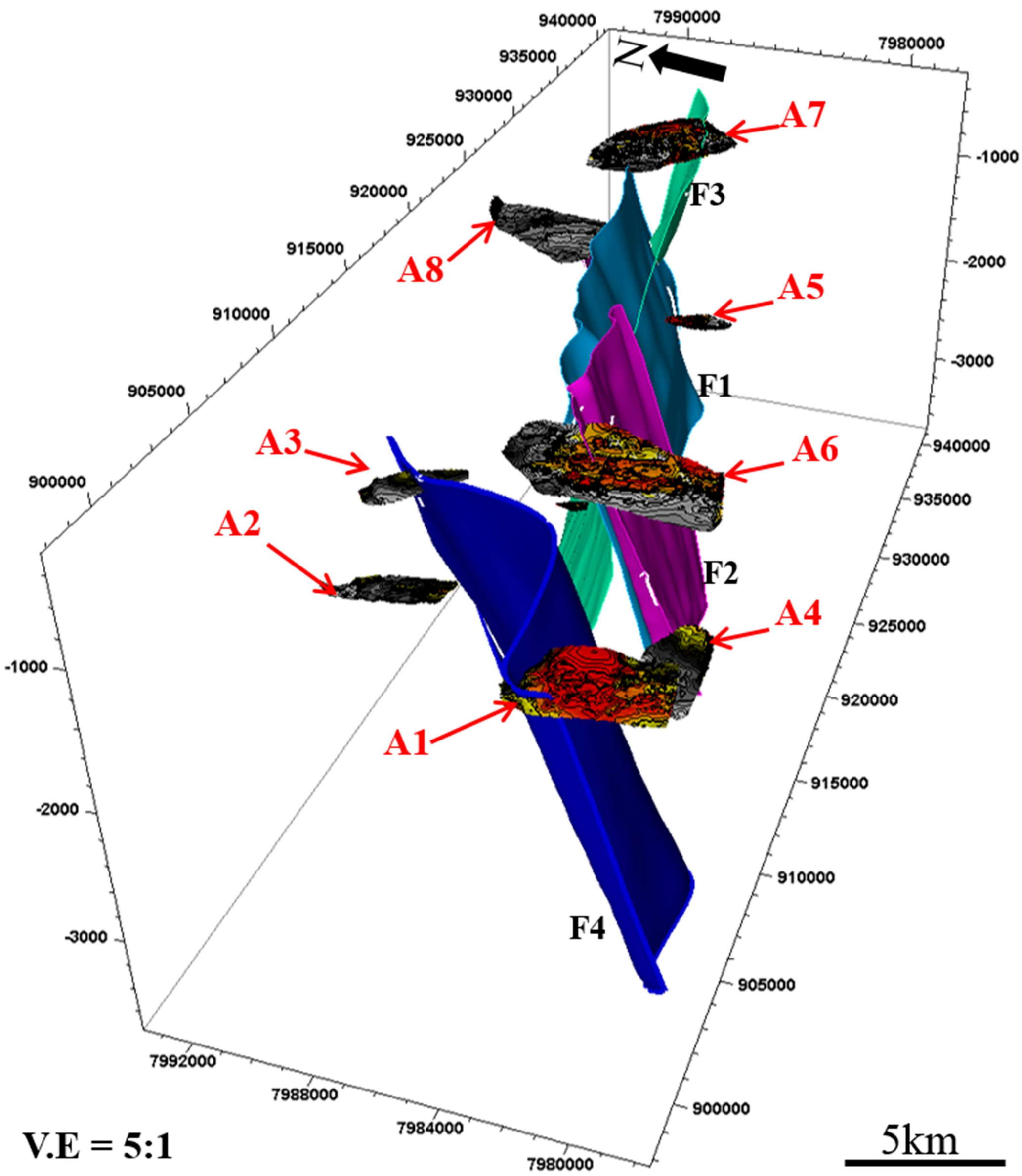

Fig. 13: The soft reflections/high-amplitude anomalies are located at the tips of the deep-seated faults. *F-Fault, A- Anomaly*.

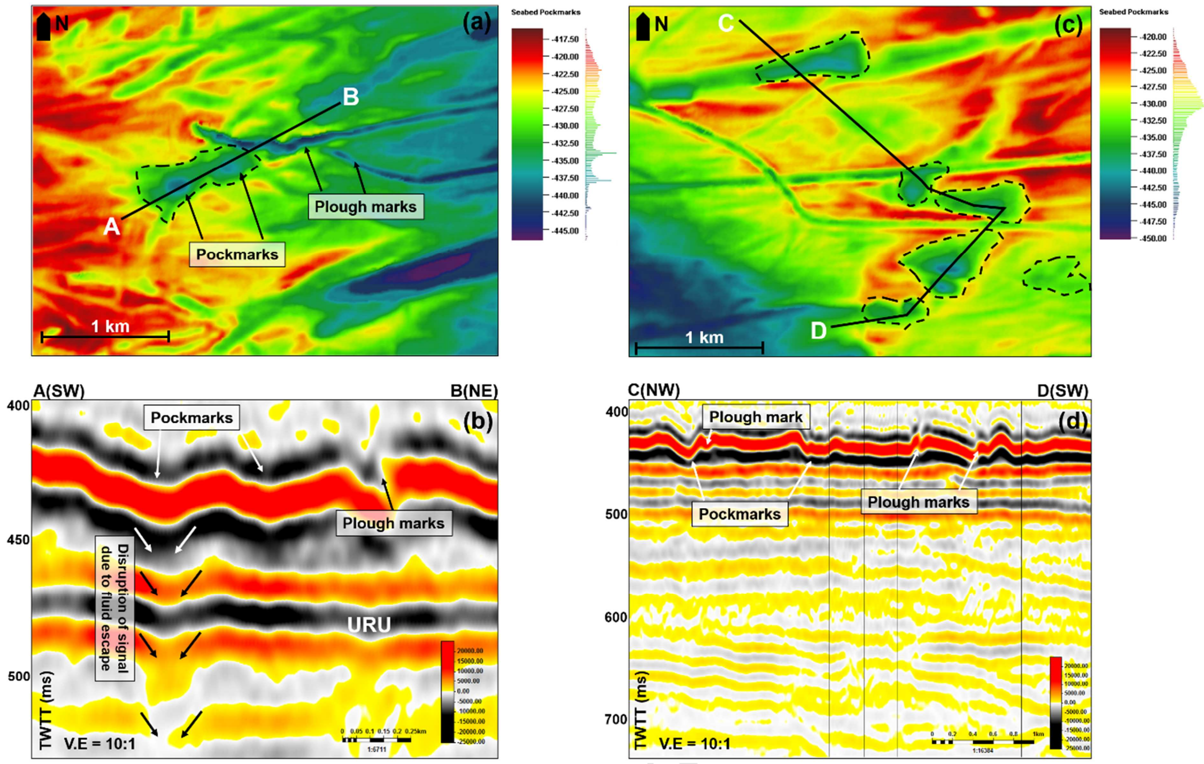

Fig. 14: Pockmarks and plough marks at the seabed (a) and (c) are structural maps of the seabed reflection while (b) and (d) are the corresponding seismic sections. *The lines of transect are shown on the maps.*

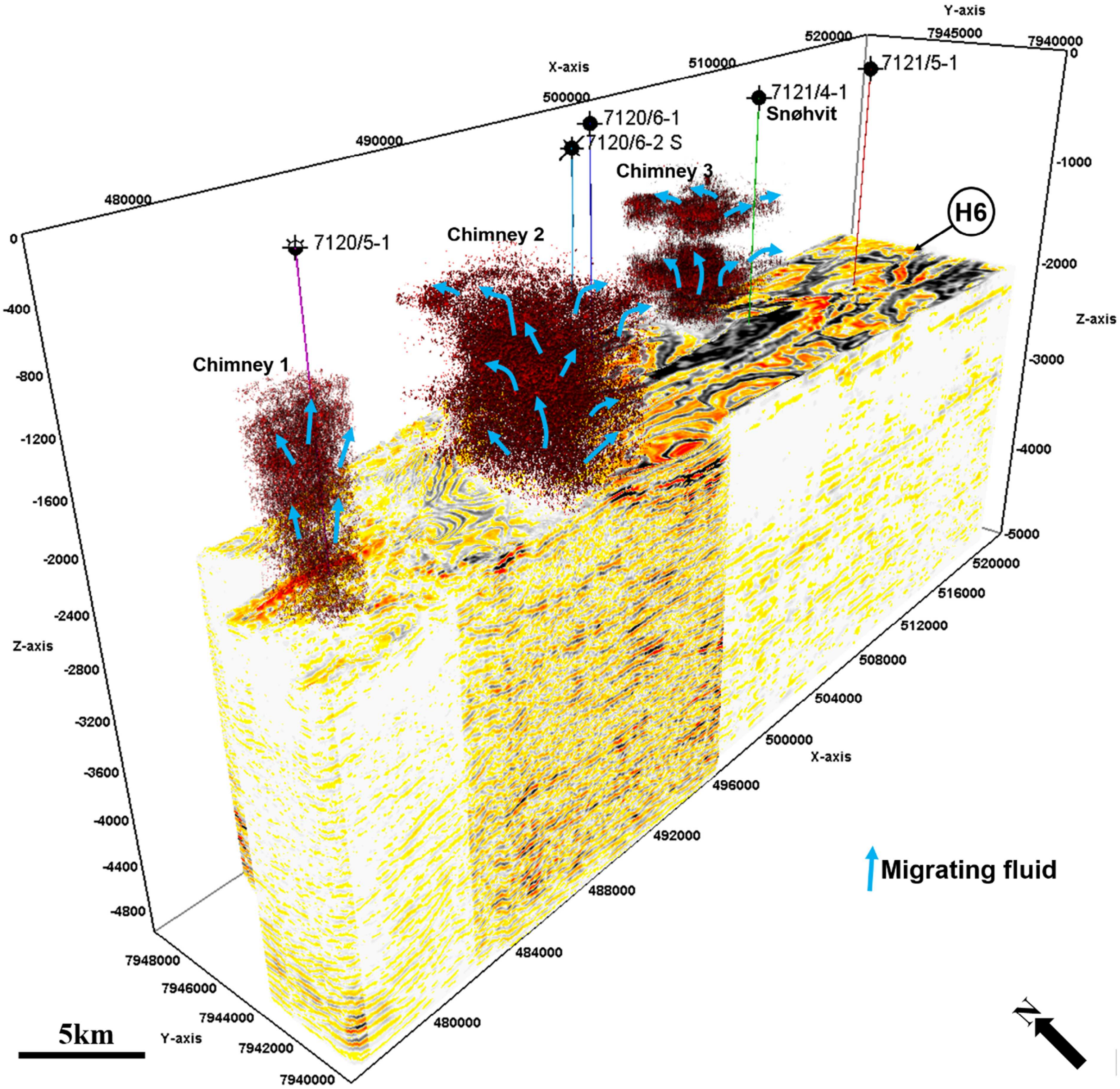

Fig. 15: Geobody extraction for the three gas chimneys showing migration of the associated fluids from deeper horizons such as H6. Chaos cube was used for mapping the gas chimneys in the study area. On the chaos cube, gas chimneys are revealed as vertical zones of chaotic to poor seismic signal when compared with the background value. Once the chimneys were identified from the chaos cube, geobody extraction was done to isolate the chimney from the rest of the seismic.

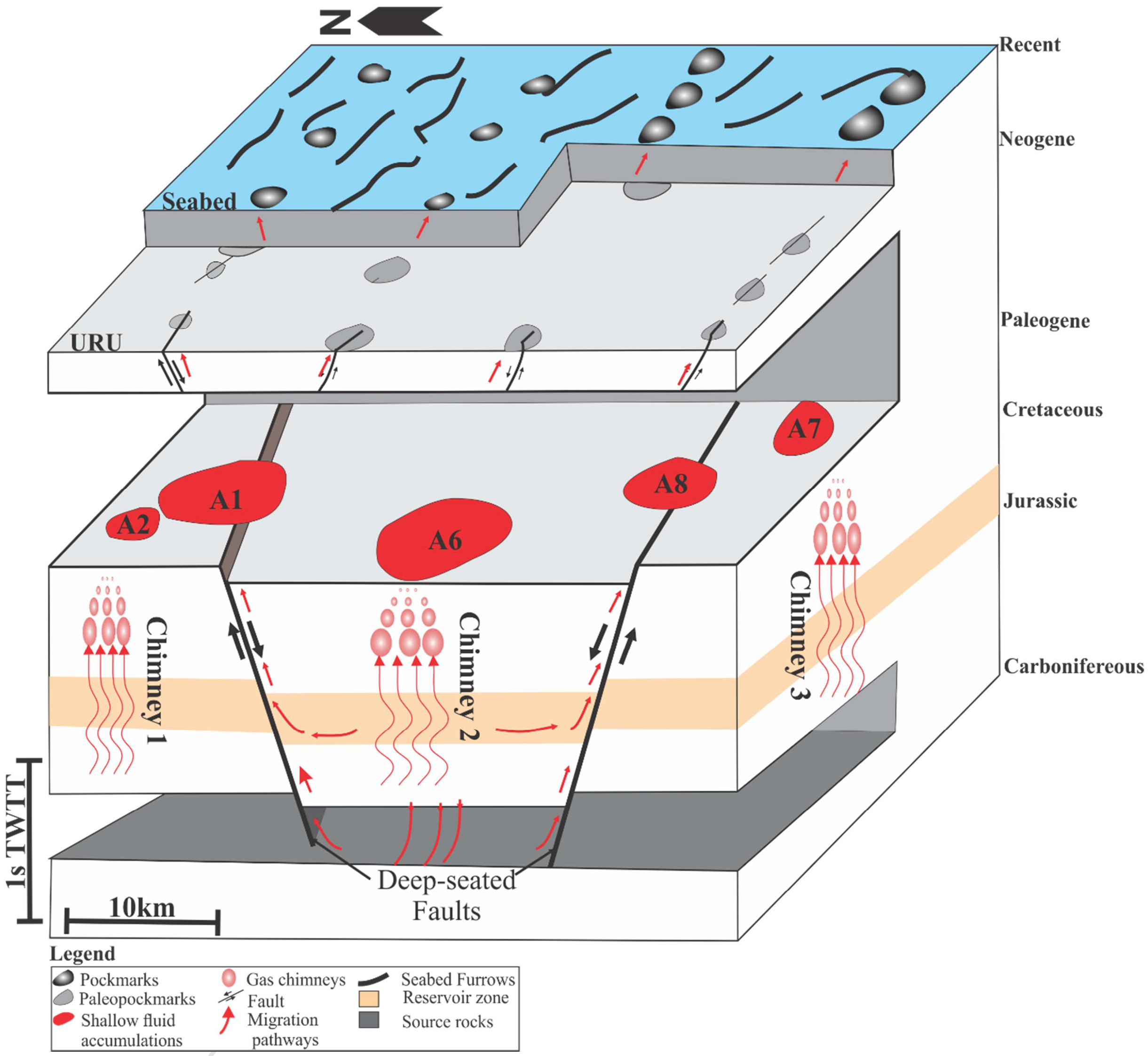

Fig. 16: Conceptual diagram illustrating the hydrocarbon plumbing system in the Snøhvit Gas Field. Also shown in the Fig. is the spatial relationship between the deep-seated faults, shallow fluid accumulations and fluid-flow features like pockmarks. The red dashed arrow indicates the migration pathways from the source to the shallow fluid accumulations. The shallow faults start approximately at the depth of the shallow fluid accumulations and linearly arranged beneath the seabed pockmarks. Hydrocarbons in the Snøhvit Gas Field are leaked from Paleozoic and Triassic source during several phases of fault reactivation. N.B: *URU is the Upper Regional Unconformity*.

- Faults in the study area are dip-slip normal faults
- Deep-seated faults in this work have complex lateral and vertical segmentation
- The deep-seated faults were reactivated in Late Jurassic, Early Cretaceous and Paleocene.
- Fluid-related anomalies show close link with the deep-seated faults
- Hydrocarbons were leaked through faults during fault reactivation.